Fundamental changes of granular flow dynamics, deposition and erosion processes at high slope angles: insights from laboratory experiments

Maxime Farin,[1] Anne Mangeney[1,3] and Olivier Roche[2]

Abstract. Entrainment of underlying debris by geophysical flows can significantly increase the flow deposit extent. To study this phenomenon, analog laboratory experiments have been conducted on granular column collapse over an inclined channel with and without an erodible bed made of similar granular material. Results show that for slope angles below a critical value θ_c, between 10° and 16°, the runout distance r_f depends only on the initial column height h_0 and is unaffected by the presence of an erodible bed. On steeper slopes, the flow dynamics change fundamentally, with a slow propagation phase developing after flow front deceleration, significantly extending the flow duration. This phase has characteristics similar to those of steady uniform flows. Its duration increases with increasing slope angle, column volume, column inclination with respect to the slope and channel width, decreasing column aspect ratio (height over length) and in the presence of an erodible bed. It is independent, however, of the maximum front velocity. The increase in the duration of the slow propagation phase has a crucial effect on flows dynamics and deposition. Over a rigid bed, the development of this phase leads to runout distances r_f that depend on both the initial column height h_0 and length r_0. Over an erodible bed, as the duration of the slow propagation phase increases, the duration of bed excavation increases, leading to a greater increase in the runout distance compared with that over a rigid bed (up to 50%). This effect is even more pronounced as bed compaction decreases.

1. Introduction

Landslides, debris flows, pyroclastic flows and snow or rock avalanches are examples of geophysical granular flows that commonly occur on steep terrain where they represent significant natural hazards to life and property. After destabilization, a granular mass tends to accelerate as gravity pulls it downslope before decelerating on gentler slopes where interaction forces dissipating energy overcome the driving force. Despite the increasing number of experimental, field and numerical studies of landslide and granular flow dynamics, the quantification of the physical processes involved and the corresponding rheological behavior of both experimental and natural flows are still open questions.

A major issue is to understand and quantify the entrainment of material on the landslide path. Indeed, material entrainment (i.e. erosion) can significantly change both deposit extent and flow dynamics, with strong implications for hazard assessment [e.g. *Sovilla et al.*, 2006; *Mangeney et al.*, 2007a, 2010; *Iverson et al.*, 2011]. Geophysical granular flows interact with their substrate in various ways depending on flow characteristics and the mechanical properties of the underlying material. Granular substrates, resulting from deposition of earlier flows or various geological events, are commonly eroded by granular avalanches [*Hungr and Evans*, 2004]. The properties of these substrates (compaction, cohesion, etc.) vary significantly depending on the materials involved and their degree of cementation after weathering. The substrate can be faulted, folded or strongly distorted, which suggests strong shear coupling at the flow base (e.g. Figure 1 of *Dufresne* [2012] and references therein). Erosion occurs preferentially on steep slopes [e.g. *Conway et al.*, 2010] but is observed as well along sub-horizontal substrates. Evidence includes entrained blocks and erosional features such as striae, furrows and impact marks [*Roche et al.*, 2013]. Particles from the substrate can also be entrained by the flow and are typically found mingled within its deposit [*Bernard and van Wyk de Vries*, 2011]. However, direct measurement of material entrainment in nature and of its link with flow dynamics is very difficult [*Sovilla et al.*, 2006; *Berger et al.*, 2011; *Schürch et al.*, 2011; *McCoy et al.*, 2013].

Attempts have been made to incorporate entrainment processes in numerical models to simulate the propagation of granular flows over erodible beds [e.g., *Mangeney et al.*, 2007a; *Bouchut et al.*, 2008; *Crosta et al.*, 2009a; 2009b; *Iverson* 2012; *Moretti et al.*, 2012]. However, given the very few observations available to constrain the models, a theoretical understanding of the entrainment processes in granular flows remains a major challenge.

In this context, laboratory experiments of granular flows are a unique way to gain insight into the erosion processes and their link with flow dynamics. Essentially, two types of analog laboratory experiments have been performed extensively over the last 15 years to investigate the behavior of geophysical granular flows. They involve: (i) the collapse of granular columns over horizontal rigid beds and (ii) steady uniform flows of granular material over inclined rigid beds generated by a constant supply upslope. By varying systematically the nature, volume, dimension and shape of the initially released mass and the substrate characteristics, granular collapse experiments over horizontal beds

[1]Institut de Physique du Globe de Paris, Equipe Sismologie, CNRS-UMR 7154, Université Paris-Diderot 7, PRES Sorbonne Paris Cité, Paris, France

[2]Laboratoire Magmas et Volcans, Université Blaise Pascal-CNRS-IRD, Clermont-Ferrand, France

[3]ANGE team, INRIA, CETMEF, Lab. J. Louis Lions

Copyright 2013 by the American Geophysical Union.
0148-0227/13/$9.00

have made it possible to establish robust scaling laws relating the characteristics of the deposit to the initial dimensions of the granular column (initial height, radius and aspect ratio, i.e. height over width) [*Balmforth and Kerswell* 2005; *Lajeunesse et al.* 2004, 2005; *Lube et al.* 2004, 2005; *Siavoshi and Kudrolli*, 2005; *Lacaze et al.* 2008]. Numerical and analytical modeling of granular collapse, using thin layer models based on empirical friction laws involving a constant friction coefficient, has been able to reproduce the deposits with their associated thin front as well as the scaling laws observed experimentally. Analytical solutions have provided insight into the empirical parameters involved in these scaling laws and have made it possible to extend them to granular collapse over inclined beds [*Kerswell* 2005; *Mangeney-Castelnau et al.*, 2005; *Mangeney et al.*, 2010]. Several granular collapse experiments have also been performed over inclined beds without trying to reproduce the scaling laws obtained on horizontal planes [*Hogg* 2007; *Mangeney et al.*, 2010; *Lube et al.*, 2011]. Furthermore, the pioneering experiments of *Pouliquen* [1999a] followed by many others have shown the existence of slow, thin, steady uniform flows with steep fronts over a range of slope inclination angles (about 20° to 28° for glass beads). Simulation of these experiments is only possible when using a friction law whose friction coefficient depends both on flow velocity and thickness [*Pouliquen*, 1999a; *Pouliquen and Forterre*, 2002; *Mangeney et al.*, 2007b]. Reconciling these two end-member types of experiments ((i) and (ii)) remains a challenge.

Experiments on granular collapse over horizontal and inclined erodible beds have been performed recently to investigate and quantify erosion processes [*Mangeney et al.*, 2007b; 2010; *Iverson et al.*, 2011; *Dufresne*, 2012; *Roche et al.*, 2013]. *Mangeney et al.* [2010] have shown that erosion processes affect the flow behavior above a critical slope angle θ_c that is about half the repose angle θ_r of the granular material ($\theta_c \simeq 12^\circ \simeq \frac{\theta_r}{2}$). At a given slope angle $\theta > \theta_c$, the runout distance in their experiments increased linearly as a function of the bed thickness, up to about 40% for inclinations close to the repose angle of the granular material involved. Three phases of flow propagation were observed: (i) an initial acceleration phase, (ii) a rapid deceleration phase and (iii) a final phase of slow propagation that appeared only at sufficiently high slope angles and/or bed thicknesses and for which the duration increased with the slope angle. The presence of an erodible bed did not affect the acceleration phase and the maximum front velocity, but it significantly increased the front velocity during the deceleration and slow propagation phases, thereby increasing the flow duration and the runout distance compared to that of collapse over a rigid bed. The experiments also showed that the penetration depth of the interface separating the flowing and static grains in the erodible bed first increased rapidly behind the flow front, reached a maximum value and finally decreased to a value that depended on the slope angle. At the interface between the erodible bed and the flow, waves of grains from the erodible bed, traveling downstream, were observed behind the flow front. How these waves affect the efficiency of erosion processes is still unclear.

Because the experiments of *Mangeney et al.* [2010] were conducted only for a rectangular granular column of aspect ratio $a = 0.7$ and volume $V = 2800$ cm^3, a channel of width $W = 10$ cm and loosely-packed beds of thickness h_i up to only 6 mm, several questions remain unresolved. Does the value of the critical angle θ_c depend on the characteristics of the released mass, the channel width and the nature of the erodible bed? Does the runout distance still increase linearly with the thickness of the erodible bed whatever the nature and thickness of the substrate and the characteristics of the released mass? What controls the increase in runout distance due to material entrainment (maximum penetration depth and/or duration of excavation, amplitude and/or duration of the waves, etc.)? Is this increase in runout distance only due to the addition of mass, i.e. would it also be obtained simply by adding this eroded mass to the initial column mass? How do the properties of the released mass (volume, aspect ratio, shape) impact on the efficiency of erosion processes and the appearance and duration of the slow propagation phase? Whatever the origin of this slow propagation phase, its strong impact on flow dynamics suggests that it represents a flow regime substantially different from the spreading regime observed for granular collapse on slopes $\theta < \theta_c$. As a result, an important question is whether the well established scaling laws observed for granular collapse over horizontal planes are still valid for flows that include a slow propagation phase. Furthermore, how does this phase compare with steady uniform flows observed over inclined planes?

To address these questions, we here investigate experimentally how, when varying initial and boundary conditions, the granular flow dynamics and erosion and deposition processes are affected by the: (i) initial aspect ratio, volume and shape of the granular column released, (ii) slope angle of the channel, (iii) channel width and (iv) thickness and degree of compaction of the erodible bed. More specifically, we investigate how runout distance, flow front velocity, duration of the slow propagation phase, deposit shape, critical slope angle θ_c, depth and duration of excavation within a flow and amplitude and duration of erosion waves vary as a function of these experimental combinations.

Section 2 describes the experimental design. After briefly presenting theoretical concepts in section 3, we test general scaling laws for granular flow runout distances in section 4 and we show the effects of various parameters on flow dynamics and deposition processes over a rigid (non-erodible) inclined bed. Section 5 deals with flows over an erodible bed and provides insights into the influence of the control parameters on flow dynamics, runout distance and erosion efficiency. Results are discussed in section 6.

2. Experimental Design

The experimental setup consisted of a 3-m-long channel bordered by smooth Plexiglas walls (Figure 1). A granular column of glass beads was released from rest at the upper end of the channel with an inclination that could be varied from 0° to about 35° (Figure 1b). The reservoir length r_0 could be varied from 10 cm to 30 cm, making it possible to release columns with different aspect ratios $a = h_0/r_0$ and volumes $V = h_0 r_0 W$, where h_0 is the height of the granular column (up to 30 cm) and W is the channel width ($W = 10$ or 20 cm).

Once released, the granular material flowed down the channel. In some experiments, the channel base was covered with a thin bed of glass beads of thickness h_i (Figure 1b). The control parameters in the apparatus were the slope angle θ, granular column aspect ratio a and volume V, as well as the thickness h_i and degree of compaction of the erodible bed. The glass beads in both the flow and erodible bed were subspherical, cohesionless and highly rigid (see Table 1 for characteristics).

The channel base was roughened by gluing a layer of the same beads on its surface. The erodible bed above that base was built using three different methods that led to an increasing degree of compaction, as described below:

1. Like *Mangeney et al.* [2010], we used the method proposed by *Pouliquen* [1999a] for the study of steady uniform flows propagating from a reservoir down a rough plane at different slope angles. By suddenly cutting the mass supply from the reservoir, a uniform thin deposit of thickness $h_s(\theta)$ was left on the rough base, forming an erodible bed (Figure 1a). In our case, for a channel width $W = 20$

cm, such deposits were observed for θ from 24.4° to 31° (Figure 2). Below 24.4°, the thickness of the deposit decreased in the downstream direction. On the other hand, for $\theta > 31°$, the flows did not form deposits, but instead left the channel. Therefore, for slope angles between 24.4° and 31°, this method generated loosely-packed beds of thickness $h_i = 1$ to 6 mm (Figure 2) with a measured volume fraction $\nu_{Pouliquen} = 0.47 \pm 0.08$ (see below). Note that a channel width $W = 10$ cm leads to thicker deposits, i.e. up to 8 mm (Figure 2). As a result, a layer of same thickness h_i is more stable on the narrow channel than on the wider channel.

2. A second method used to generate an erodible bed consisted of using a sliding board to level a layer of beads initially poured on a horizontal rough plane, then slowly increasing the slope angle. This process compacted only the free surface of the layer with a thickness of ~ 8 to 12 grain diameters (i.e. ~ 5 to 8 mm) whereas the lower layer remained relatively uncompacted, thereby leading to beds of mean volume fraction $\nu_{board} = 0.65 \pm 0.08$, which decreased with increasing bed thickness.

3. A third method used to create erodible beds generated the highest degree of compaction ($\nu_{vib} = 0.74 \pm 0.03$). After the bed was leveled with a board as in the second method, it was vibrated by gently tapping each side of the channel 10 times to compact the beads.

The solid volume fraction ν of each erodible bed was measured by removing and weighing a section of length l and thickness h_i from each bed. The volume $h_i l W$ of this bed slice was compared to the volume of grains m/ρ_b, where m and ρ_b are respectively the mass of material and density of the individual beads in the slice. The solid volume fraction is then given by $\nu = m/(h_i l W \rho_b)$.

We performed a series of experiments in which the length of the deposit r_f from the gate at $x = 0$ (the runout distance), the final thickness of the deposit at the upper wall h_f and the time t_f at which the front stopped (Figure 1b) were measured systematically, except for cases in which the granular flow did not stop on the plane and left the channel. Runout distances of flows over erodible beds were reproducible to within 3 cm, corresponding to a variation of at most 8% of the runout distance. The thickness $h(x,t)$ and front velocity $V_f(t)$ of the flow were determined from high-speed videos. In all experiments, the gate was removed rapidly (at ~ 2 m s^{-1}) over a time scale much shorter than the flow duration. Thus, our experiments were equivalent to an instantaneous dam-break process.

Experiments were first carried out on a rigid, rough channel for slope angles ranging from $\theta = 0°$ to 24° and volumes from $V = 1400$ cm^3 to 12600 cm^3. Aspect ratios a ranged from $a = 0.3$ to 1.24, consistent with many geophysical flows [e.g. *Mangeney et al.*, 2012]. Most experiments were performed in a 20-cm-wide channel but some experiments were also conducted in a 10-cm-wide channel to quantify the influence of the channel width on our results (Experiments **E'** in Table 2). Experiments were then repeated with the same initial and boundary conditions, but with the channel covered by a thin erodible bed of variable thickness $h_i =$ 1 to 25 mm (Table 2). In natural cases, the initial shape of a destabilized mass is generally not rectangular. Therefore, trapezoidal reservoirs, with the gate inclined at 70° with respect to the horizontal (Figure 1b), were considered in addition to rectangular reservoirs with the gate perpendicular to the channel base. For the same volume V, the initial column height h_0 and the initial column length r_0 were both greater for a trapezoidal reservoir than for the rectangular reservoir. However, to compare results between reservoir shapes, we also defined the aspect ratio a of the trapezoidal column as the ratio of h_0 to r_0 (Figure 1b). The trapezoidal reservoirs allowed us to release columns of volume $V = 12600$ cm^3 and aspect ratio $a = 0.7$ onto slopes having angles between 0° and 24° with respect to the horizontal (Experiments $\mathbf{E}^t$ in Table 2).

In order to observe velocity profiles on one side of the flow (through the transparent channel wall) and estimate the evolving interface separating flowing and static grains, we used black beads as tracers at a volume fraction of about 50%. Black beads had a slightly higher repose angle ($\theta_{rb} \simeq 25°$) than the regular beads ($\theta_r \simeq 23°$), possibly due to slight cohesion effects caused by the ink used to color the beads. To investigate how the amplitude and duration of erosion waves varied as a function of the aspect ratio a and volume V, we performed experiments with an erodible bed made of colored black beads. To obtain sufficient accuracy, it was necessary to work at high slope angles close to the friction angle of the glass beads, typically $\theta \geq 19°$. At such angles, the wave amplitude and the excavation depth in the erodible bed were expected to be maximized.

3. Theoretical Model for Granular Flow Dynamics

To provide a basis for interpreting our experimental results, we review a theoretical framework describing the behavior of dry granular flows. The dynamics of granular flow result from a complex balance between inertia, gravity, friction and pressure gradients. *Savage and Hutter* [1989] described granular flows using a hydrodynamic approximation by averaging the 3D equations of mass and momentum conservation throughout the flow depth, assuming that the flow has a length much greater than its thickness. This is the case for most geophysical flows that are a few meters thick and travel distances of several hundred meters to several kilometers. The flow is also assumed to be incompressible and of constant density ρ. In this so-called shallow layer approximation, the flow is described by its local thickness $h(x,y,t)$ and its depth-averaged downslope velocity $\mathbf{u}(x,y,t) = u\mathbf{e}_x + v\mathbf{e}_y$, where x and y are the downslope coordinates in the reference frame of the slope (Figure 1b) and t is time. Assuming 2D flow, the equations of conservation of mass and momentum are:

$$\frac{\partial h}{\partial t} + \frac{\partial hu}{\partial x} = 0, \tag{1}$$

$$\rho\left(\frac{\partial hu}{\partial t} + \frac{\partial hu^2}{\partial x}\right) = \rho g h \cos\theta(\tan\theta - \mu(h,u) - K\nabla\cdot h), \tag{2}$$

where g is gravitational acceleration, θ the slope angle and K the ratio of vertical to horizontal normal stress [*Savage and Hutter*, 1989]. In equation (2), acceleration (left hand term) is balanced by three forces (right hand terms): (i) gravity, which is the driving force for the flow, (ii) friction, which opposes the motion and is proportional to the friction coefficient μ and to the vertical normal stress $\rho g h \cos\theta$; and (iii) the force related to the pressure gradient, which involves the thickness gradient $\nabla \cdot h$.

Assuming a Coulomb friction law, i.e. a constant friction coefficient $\mu = \tan\delta$, with δ the friction angle of the granular material, we introduce dimensionless variables by scaling the downslope distance x and flow depth $h(x,t)$ using the initial column length r_0 and height h_0 [*Roche et al.*, 2008; 2011; *Mangeney et al.*, 2010]. Downslope velocity u is scaled by $\sqrt{K g cos\theta h_0}$ and time t is scaled by $r_0/\sqrt{K g cos\theta h_0}$ [e.g. *Kerswell*, 2005; *Mangeney-Castelnau et al.*, 2005; *Hogg*, 2007]. The resulting dimensionless equations are:

$$\frac{\partial \tilde{h}}{\partial \tilde{t}} + \frac{\partial \tilde{h}\tilde{u}}{\partial \tilde{x}} = 0, \tag{3}$$

$$\frac{\partial \tilde{u}}{\partial \tilde{t}} + \tilde{u}\frac{\partial \tilde{u}}{\partial \tilde{x}} + \nabla\cdot\tilde{h} = -\frac{\epsilon}{K}. \tag{4}$$

where ϵ is a dimensionless parameter defined by

$$\epsilon = \frac{\tan\delta - \tan\theta}{a}, \tag{5}$$

with $a = h_0/r_0$, the column aspect ratio. This model describes dry granular flows over a simple, linear inclined plane. More complex models have been developed to simulate dense granular flows over realistic 3D topographies [e.g. *Denlinger and Iverson*, 2001; *Bouchut et al.*, 2003; *Bouchut and Westdickenberg*, 2004; *Denlinger and Iverson*, 2004; *Mangeney et al.*, 2007b].

4. Granular Flow over an Inclined Rigid Bed

4.1. Scaling Laws for Runout Distance

In the literature, the runout distance r_f is typically scaled by dividing it by the initial column length r_0 or height h_0. Experimental results of rectangular [*Balmforth and Kerswell*, 2005; *Lajeunesse*, 2005; *Lube*, 2005] and axisymmetric [*Lajeunesse*, 2004; *Lube*, 2004] column collapse on a horizontal plane reveal that the ratio r_f/r_0 increases linearly with the column aspect ratio a and is independent of the volume V, for small aspect ratios ($a < 0.7$ to 3, depending on the configuration). Hence, the runout distance r_f is proportional to the initial column height h_0. Using numerical and analytical solutions of equations (3) and (4), *Kerswell* [2005] and *Mangeney-Castelnau et al.* [2005] also predict that the ratio r_f/r_0 is proportional to a (regardless of a and for $a < 1$, respectively). *Mangeney et al.* [2000, 2010] developed an analytical expression for granular flow over an inclined plane:

$$\frac{r_f}{h_0} = \frac{2k}{\tan\delta - \tan\theta} \tag{6}$$

where the value of the coefficient k was empirically set to 0.5 [*Mangeney et al.*, 2010] and δ is an empirical friction angle. Equation (6) shows that the runout distance r_f, normalized by the initial column height h_0, is inversely proportional to the difference between the tangent of the slope angle θ and the tangent of the friction angle δ of the material.

We report flow runout distances in our experiments at various slope angles and examine whether they satisfy the scaling laws established in the literature for horizontal beds and if the results can be successfully fitted by equation (6) when the slope angle θ increases.

For slope angles $\theta \leq 16^\circ$, runout distances r_f satisfy the same scaling laws as those obtained for the horizontal case; r_f is proportional to h_0 (Figure 3a) and normalized runout distances r_f/r_0 are independent of V and increase linearly with a (Figures 3b and 3c). The best fit of equation (6) to our data is obtained using $\delta = 27^\circ$, slightly higher than the angle of repose measured experimentally ($\theta_r \sim 23^\circ$) [e.g. *Mangeney-Castelnau et al.*, 2005; *Kerswell*, 2005; *Hogg*, 2007]. For $\theta \leq 16^\circ$ (i.e. $1/(\tan\delta - \tan\theta) \leq 4.5$), equation (6) provides a good prediction of the runout distance r_f of granular flows: for a given slope angle θ, all the values of r_f/h_0 collapse, regardless of the aspect ratio a (Figure 4a) and the volume V (Figure 4b).

On the other hand, these scaling laws are not applicable for flows on slope angles $\theta > 16^\circ$. At such angles, r_f does not depend on h_0 only, but instead clearly depends on the volume V (i.e. r_0) (Figure 3a). This result has never before been reported. For $a = 0.7$, r_f/r_0 increases with the volume V and even more so when the slope angle θ increases (Figure 3b). For example, for $\theta = 23^\circ$ and $a = 0.7$, r_f/r_0 varies from 5.6 to 7.7 for volumes V ranging from 1400 cm^3 to 12600 cm^3. For a given slope angle $\theta > 16^\circ$ (i.e. $1/(\tan\delta - \tan\theta) > 4.5$), values of r_f/h_0 diverge from the theoretical trend when varying the aspect ratio a and the volume V (Figures 4a and 4b). As a result, the analytical expression (6) is no longer appropriate to describe the dependence of the runout distance on volume and aspect ratio for slope angles higher than 16°.

The runout distance is also sensitive to channel width W and to column initial shape (i.e. rectangular or trapezoidal), even for small slope angles θ. Normalized runout distances r_f/h_0 are systematically greater when the channel is wider and are slightly smaller for the trapezoidal column than for a rectangular column of the same volume $V = 12600$ cm^3 and equivalent aspect ratio $a = h_0/r_0 = 0.7$ (Figure 4c).

Hogg [2007] carried out column collapse experiments on a rigid, 30-cm-wide inclined channel and used different types of material that included Ballotini beads (diameter $d = 100$ μm and 350 μm) and PVC powder ($d = 140$ μm) (Figures 3d, 3e and 4d). Since *Hogg* [2007] used different control parameters (θ, a, V, W, type of material) than ours, we cannot quantitatively compare the runout distances r_f between the two studies. However, if we use friction angles of 2° higher than the angles of repose he measured experimentally for the different materials, the data of *Hogg* [2007] support our qualitative observations. In these experiments, the normalized runout distances r_f/h_0 match the empirical equation (6) well only until $1/(\tan\delta - \tan\theta) \simeq 6$ (Figure 4d), in agreement with our results. The influence of the volume V on r_f/r_0 for a given $a = 0.5$ or $a = 1$ clearly appears for high slope angles $\theta \geq 18^\circ$ and is even more significant as θ increases (Figures 3d and 3e).

4.2. Temporal Evolution

We investigate the influence of the initial aspect ratio, volume and shape of the column on flow dynamics and deposit geometry of a mass released over an inclined rigid bed of slope angle θ between 0° and 24°. $\theta = 24^\circ$ is the highest angle of bed inclination for which a flow deposited on the plane; for higher inclinations, the granular material flowed beyond the experimental channel. Parameter values for these experiments are given in Table 2.

4.2.1. Thickness Profiles

The flow thickness profile and deposit geometry depend on the column aspect ratio a, volume V and initial shape (Figure 5). For high slope angles, typically $\theta = 22^\circ$, and for a given volume V, the thickness profile over the first 60 cm of length is similar for every aspect ratio a. Thereafter a steeper front is observed for smaller aspect ratios (Figures 5a to 5d). For a given $a = 0.7$, the front has a similar shape for every volume V until about 0.3 s of propagation. The profile then becomes more parallel to the slope and has a steeper front as volume V increases (Figures 5e to 5g). With a trapezoidal column, the flow front first propagates more slowly than with a rectangular column. Ultimately, the front from the trapezoidal column catches up with that from the rectangular column ($t \simeq 1$s) and leads to a deposit that is longer, but with a less steep front (Figures 5g and 5h). Note that the flow profile at $t = 0.18$ s in Figure 5d shows that some grains are entrained vertically by the gate uplift, as already observed by *Lube et al.* [2007] and *Mangeney et al.* [2010]. Although gate removal may affect the first few tenths of seconds of collapse of high columns, it does not seem to have a major influence on the overall dynamics of the flow or on the runout distance.

The geometry of the flow deposit changes as the slope angle θ increases. For flows along a horizontal channel, the final thickness profiles scaled by deposit dimensions h_f and r_f are independent of the volume V, for a given aspect ratio a (Figure 6b), which agrees with the results of 2D and 3D experiments [*Balmforth and Kerswell*, 2005; *Lajeunesse et al.*, 2004; 2005]. In contrast, for a given volume V, the final thickness profile depends on the aspect ratio a: at the upstream confining wall, the profiles show an undisturbed plateau of thickness h_0 and decreasing downslope length for increasing a (Figure 6a). There is no plateau for $a = 1.24$, a result that is in good agreement with the theoretical results

of *Kerswell* [2005]. The deposit profiles on a horizontal plane also seem to depend slightly on the initial column shape: with the trapezoidal column, the deposit profile does not have an undisturbed plateau (Figure 6c). The front shape is, however, similar to that of the deposit obtained with a rectangular column of the same aspect ratio a and volume V. In contrast, for greater slope angles, typically $\theta = 22^\circ$ (Figures 6d to 6f), the fronts of the final normalized profiles are steeper than for $\theta = 0^\circ$ (Figures 6a to 6c), as observed by *Mangeney et al.* [2010]. For a given V, the fronts of the final profiles are steeper for smaller aspect ratios but are flatter and more concave-upward for higher aspect ratios, typically $a = 1.24$ (Figure 6d). For a given a, the profiles are more curved and the fronts are steeper as V increases (Figure 6e), as in the experiments of *Hogg* [2007] for $a = 0.5$ and different values of V. At $\theta = 22^\circ$ with a trapezoidal column (Figure 6f), the deposit front also exhibits a steep shape. The deposit profile is more curved and the front less steep than the one obtained with a rectangular column.

4.2.2. Flow Front Dynamics

The flow front dynamics change critically for slope angles $\theta \geq 16^\circ$ compared to smaller slopes because a regime of slow propagation develops at the end of the deceleration phase, which significantly increases the duration of the front propagation and the flow runout distance (Figures 7a to 7c). For slope angles $\theta < 16^\circ$, there is no slow propagation phase (Figure 7c). After the front stops, some mass movement from the upstream confining wall to the front is still observed. This mass movement reshapes the deposit profile but does not affect the flow extent (for example for $\theta = 0^\circ$ in Figures 8a and 8b).

At $\theta > 16^\circ$, the duration of the slow propagation phase increases as the slope angle θ and volume V increase and as the aspect ratio a decreases (Figures 7a to 7c, 8c and 8d). For flows at $\theta = 22^\circ$ and $V = 5600$ cm^3, the slow propagation phase lasts approximately 1.9 s for $a = 0.3$ and it is not observed for $a = 1.24$ (Figures 7a and 8c). As a consequence, the total duration of propagation for $\theta = 22^\circ$ is longer for small than for high aspect ratios, in contrast to what is observed in the horizontal case for which there is no final slow propagation regime (Figures 8a and 8c). The slow propagation phase is still present but its duration is shorter when the initial column shape is trapezoidal rather than rectangular (Figure 7c). With the column dimensions $h_0 = 14$ cm and $r_0 = 20$ cm, the slow propagation phase lasts about 0.2 s longer in the 20-cm-wide channel than in the 10-cm-wide channel of *Mangeney et al.* [2010]. For slope angles $\theta > 16^\circ$, the rear of the mass stops before the front so that when the front stops, the whole mass is at rest.

In contrast to the slow propagation phase, the initial front acceleration – that is the slope of the tangent to the velocity profile $V_f(t)$ at $t = 0$ – is independent of slope angle θ and does not depend on aspect ratio a or on volume V (Figures 7a to 7c). It clearly depends, however, on the initial column shape because acceleration following release of the trapezoidal column is only half that following release of the rectangular column of the same dimensions (Figure 7c). Furthermore, the duration of the acceleration phase increases slightly with θ, a and V but lasts twice as long for the trapezoidal column collapse (Figures 7a to 7c). The maximum front velocity V_{fm} is proportional to $\sqrt{gh_0 \cos\theta}$ (Figure 7d) [e.g. *Roche et al.*, 2008]. Several experiments for $\theta = 22^\circ$, at a constant column height $h_0 = 14$ cm (i.e. $\sqrt{gh_0 \cos\theta} \simeq 112$ cm s^{-1}) and different column lengths r_0 from 10 cm to 30 cm, reveal that V_{fm} does not depend on r_0 (Figure 7d). Furthermore, the maximum front velocity V_{fm} appears not to depend on the column initial shape (i.e. trapezoidal or rectangular, Figure 7c).

5. Flow over an Inclined Erodible Bed

5.1. Critical Angle and Runout Distance

We now investigate flow runout over an inclined erodible bed. *Mangeney et al.* [2010] showed that there is a critical angle $\theta_c \simeq \frac{\theta_r}{2}$ above which the runout distance over an erodible bed increases compared to the runout distance over a rigid bed. Our new data show that this critical angle θ_c is between $\theta = 10^\circ$ and 16° regardless of the column aspect ratio a, volume V and shape (Figure 9). The lack of data between $\theta = 10^\circ$ and 16° does not allow us to determine the critical angle more precisely. For $\theta \leq 10^\circ$, the normalized runout distance r_f/h_0 does not change for flows over an erodible bed (i.e. $h_i > 0$ mm) with respect to a rigid bed (i.e. $h_i = 0$ mm). For $\theta \geq 16^\circ$, the runout distance is affected by the presence of an erodible bed: as the bed thickness h_i increases, the normalized runout distance r_f/h_0 first increases and then stabilizes at a maximum value (for $\theta = 16^\circ$ - 19°) or sometimes decreases slightly, for example when $\theta \geq 22^\circ$ (Figures 9a and 9b).

The increase in runout distance over an erodible bed depends on θ, a, V, column shape and channel width W (Figures 9a and 9b). The differences in runout distances over an erodible compared to a rigid bed were calculated for the experiments in Figures 9a and 9b. The maximum runout distance difference Δr_{fmax} increases with the slope angle θ up to about 50% for $\theta = 23^\circ$ (Figures 9c to 9f). There is an exception, however, for $\theta = 22^\circ$, $V = 5600$ cm^3 and $a = 1.24$ (Figure 9c), where Δr_{fmax} is smaller than for $\theta = 19^\circ$. This value comes from a one-time experiment and plots within the $\pm 4\%$ error bars. For this specific experiment, the runout distance r_f increases by at most 4% as the bed thickness h_i increases and even slightly decreases for $h_i > 15d$ (Figure 9a). In contrast, r_f can increase by up to 32% for smaller aspect ratios a, at the same slope angle $\theta = 22^\circ$ (Figure 9e). For $a = 0.7$, the maximum runout distance difference Δr_{fmax} clearly increases with the column volume V and even more so as the slope angle θ approaches the repose angle θ_r of the granular material (Figure 9d). For granular flows generated from a trapezoidal column or in the 10-cm-wide channel, the runout distance increases less in the presence of an erodible bed than for a rectangular column of similar dimensions or a wider channel ($a = 0.7$ and $V = 12600$ cm^3, Figure 9b).

The degree of compaction of the erodible bed has a substantial impact on the flow runout distance, particularly in steep channels (Figure 10). For a given slope angle, the normalized runout distance r_f/h_0 is systematically greater on a loosely-compacted bed than over more compacted beds. For $\theta = 22^\circ$, where erosion is clearly observed, the least compacted, loose bed (*Pouliquen* method) leads roughly to a linear increase of r_f/h_0 with the bed thickness h_i, a result observed by *Mangeney et al.* [2010]. For more compacted beds, when h_i increases, r_f/h_0 first increases, tends toward a maximum value for h_i between $4d$ and $24d$ and then decreases. The board method compacts mostly the top of the bed while the grains underneath remain relatively undisturbed. With the vibration method, the compaction is homogenous throughout the bed thickness. Furthermore, the upper part of beds created with the board may be more compact than the beds compacted by vibrations. Thin beds ($h_i < 15d$) may then be more compact when using the board. In contrast, the mean solid volume fraction of thicker beds becomes smaller when they are build with the board than with the vibration method, since the lower undisturbed layer of the bed is thicker, as opposed to the highly compacted upper layer. Consequently, on thin beds, values of r_f/h_0 are greater with the vibration method than with the board method until $h_i \simeq 8d$ to $15d$ and then decrease as the bed thickness increases (Figure 10).

5.2. Entrainment vs Mass Addition

During collapse, the flow excavates the underlying granular bed from which some beads are extracted and entrained (Figure 11) [see also *Mangeney et al.*, 2010; *Rowley et al.*, 2011; *Dufresne*, 2012; *Estep and Dufek*, 2012]. At a given distance x from the gate, the position $h_{F/S}$ of the interface that separates the flowing and static grains within the erodible bed deepens rapidly after the passage of the flow front, reaching a maximum depth h_C, and then becomes shallower towards $h_{F/S} = 0$ (Figure 11). Entrainment of the upper part of the erodible bed by the flow can increase the runout distance on slopes θ larger than 10° to 16° (Figure 9). We wanted to check whether it was possible to obtain the same runout distance over a rigid bed simply by adding the entrained mass to the initial column.

In order to test this possibility, we estimated the volume V_m of the initially static beads entrained by the flow. The erodible bed was assumed to have been excavated over a thickness equal to the maximum excavation depth h_C along the runout distance r_f and across the channel width W. Our estimation of the maximum entrained volume is therefore $V_m = h_C r_f W$. Note that this is an upper bound since the excavation depth h_C was not constant along the channel (see section 5.4). We then conducted experiments in which we added the volume V_m to the initial volume in the reservoir V_i and released this new volume $V = V_i + V_m$ over the rigid bed (Figure 12). The runout distance of avalanches of larger volume $V = V_i + V_m$ over a rigid bed was always smaller than that of similar flows of volume V_i over erodible beds (Table 3). For example, for $\theta = 22°$, $a = 1$, $V_i = 2000$ cm^3 and $h_i = 8$ mm, the erodible bed was excavated over a depth $h_C = 3$ mm along the runout distance ($r_f = 84$ cm). The volume of erodible bed entrained was therefore $V_m = h_C r_f W = 0.3 \times 84 \times 20 = 504$ cm^3 (i.e. about 1/4 of the total volume). In contrast, the runout distance of the flow of volume $V = V_i + V_m = 2000 + 504 = 2504$ cm^3 over the rigid bed was about 7% smaller than that over the 8-mm thick bed. Hence, these experiments demonstrate that the increase in the runout distance caused by an erodible bed is not solely due to a mass increase. The presence of an erodible bed somehow fundamentally changes the dynamics of the granular flow.

5.3. Effect of an Erodible Bed on the Flow Dynamics and Deposit Characteristics

5.3.1. Thickness Profiles

The flow thickness profile over an erodible bed is similar to that over the rigid bed during initial spreading ($t < 0.3$ s, Figure 13). However, as the flow spreads away from the gate, the free surface of the profile becomes almost parallel to the slope ($t > 0.3$ s, Figure 13). The deposit profiles over an erodible bed are more concave upward than over a rigid bed, except for $V = 1400$ cm^3 (compare Figures 6d and 14a and Figures 6e and 14b). The concavity is more pronounced for greater aspect ratios a and volumes V (Figures 14a and 14b). In those thickness profiles, a transition from upwards concavity to convexity can be clearly identified at the front of the deposit, for $x/r_f \simeq 0.7$ to 0.8.

For the horizontal case ($\theta = 0°$), the erodible bed has an effect on the deposit geometry. The deposit profile does not have a plateau at the upstream confining wall and has a slightly steeper front than over a rigid bed, as if more mass was transported from the rear towards the flow front (Figure 14c). With a trapezoidal column, the front is steeper than with a rectangular column (Figure 14d), contrary to what was observed over the rigid bed (Figure 6f).

5.3.2. Flow Front Dynamics

Mangeney et al. [2010] reported that most of the increase in runout distance over an erodible bed is acquired during the deceleration and slow propagation phases. The present experiments show that this is true regardless of column aspect ratio a, volume V and shape, slope angle θ and bed thickness h_i (Figure 15). The amplitude and duration of the front acceleration phase and the maximum front velocity V_{fm} of flows over an erodible bed do not change compared to those over a rigid bed (Figures 7a, 7b, 15a, 15b and 15e). The maximum front velocity V_{fm} is still scaled by $\sqrt{gh_0 \cos\theta}$ (Figure 7d). In contrast, during the deceleration phase, the flow front velocity is greater over an erodible bed than over the rigid bed (Figure 15e). Furthermore, the slow propagation phase of flows over an erodible bed lasts globally longer than over the rigid bed (Figures 15f and 15g) and its duration corresponds to a greater proportion of the total duration of propagation ($t_{spp}/t_f = 50 - 70\%$), particularly for high aspect ratios a (Figures 15h and 15i). As a result, the difference in the front positions Δx_f with respect to the rigid bed case starts to increase at the beginning of the deceleration phase (except for $a = 1.24$, Figures 15c) and then continues to increase, although more slowly, during the slow propagation phase (Figures 15c and 15d). For $a = 0.7$, up to 80% of the runout distance increase Δr_f takes place during the slow propagation phase for the greatest volumes V investigated (Figure 15d). For a given volume $V = 5600$ cm^3, the slow propagation phase corresponds to ~ 35 to 42% of the runout distance increase Δr_f for small aspect ratios a whereas it represents 100% of Δr_f for high column aspect ratios such as $a = 1.24$ (Figure 15c). For this specific experiment, the flow front traveled a longer distance over the rigid bed than over the erodible bed at the end of the deceleration phase (i.e. $\Delta x_f < 0$, Figure 15c). Because a slow propagation phase is not present over the rigid bed but develops over the erodible bed (Figures 7a and 15a), the front reaches ultimately a longer runout distance than over the rigid bed (Figure 15c).

Pouliquen [1999a] presented a scaling law relating front velocity V_f to thickness h of steady uniform flows at a given slope angle θ:

$$\frac{V_f}{\sqrt{gh}} = \beta \frac{h}{h_s(\theta)} \tag{7}$$

where $h_s(\theta)$ is the deposit thickness at slope angle θ (see section 2 and Figure 2) and β is an empirical parameter equal to 0.136 for glass beads. We tested this scaling law for our granular flows in the slow propagation phase using V_{fmean}, the mean front velocity during the slow propagation phase and h_{mean}, the mean thickness of the flow behind the front. When the slow propagation phase lasts sufficiently long (> 1s), i.e. for small aspect ratios $a \leq 0.7$ and great volumes $V \geq 8750$ cm^3 over the rigid bed, and for all flows over an erodible bed (Figures 15f and 15g), the flow characteristics match the scaling law (7) well (Figure 16a). As a result, the flow law (7) is more valid for flows over an erodible bed for which the slow propagation phase lasts longer than over the rigid bed (Figures 15f, 15g and 16a).

The mean thickness h_{dmean} of the portion of the deposit that is quasi-parallel to the slope in the experiments presented in Figures 5 and 13 is shown to increase when the duration of the slow propagation phase increases and seems roughly to saturate for flows with a well developed slow propagation phase ($t_{spp} > 1.2$ s and $t_{spp} > 1.6$ s for $\theta = 22°$ and $\theta = 23°$, respectively, Figures 16b and 16c). The maximum value of h_{dmean} is smaller when the slope angle θ increases. For example, it is 1.65±0.1 cm for $\theta = 22°$ (Figure 16b) and 1.35±0.1 cm for $\theta = 23°$ (Figure 16c). These maximum values are reported in Figure 2.

5.4. Insight into Erosion Processes

The presence of an erodible bed has the most significant influence on flow mobility at slope angles greater than 10° to

16° (Figure 9) and during the deceleration and slow propagation phase (Figure 15). We decided to investigate whether bed erosion was deeper and longer during these phases and how this can be related to the increase in the runout distance over an erodible bed. For this, we measured the position of the flowing/static interface $h_{F/S}(t)$ (Figure 11) and the velocity profile $u(y)$ on one side of the flow (through the transparent channel wall) at different positions x from the gate to observe their variations during flow propagation, for the specific experiment where $\theta = 23°$, $a = 0.3$ and $V = 5600$ cm^3 (Figure 17). Furthermore, the maximum excavation depth h_C and duration of bed excavation t_d were measured at the position where the front velocity V_f was maximum in order to be compared for different initial and boundary conditions that influence the runout distance increase (Figures 18 and 19). We considered that a particle was mobilized when its downslope velocity exceeded 10 mm s^{-1}. Measurements were done on slope angles $\theta \geq 19°$ for which bed entrainment is expected to be high and the depth and duration of excavation may be easily measured.

During the acceleration phase (for $\theta = 23°$, $a = 0.3$ and $V = 5600$ cm^3; Figures 17a and 17b), the bed is excavated deeply ($h_C \simeq 5.1d$) and with a high excavation velocity ($\frac{dh_{F/S}}{dt} \simeq 33$ mm s^{-1}), but only over a very short time ($t_d \simeq 0.4$ s). As the front spreads away from the gate (Figures 17c to 17f), the maximum depth of excavation h_C and excavation velocity decrease whereas the time t_d during which the bed is excavated increases until a position x between 100 cm and 160 cm during the slow propagation phase when it finally decreases (Figures 17e and 17f). Regardless of the measurement position x, the velocity within the flow $u(y)$ increases with the elevation y above the channel base (Figures 17g to 17k). This increase is first exponential above the flowing/static interface (i.e. $u(y) = 0$), then becomes linear for higher y and, in some cases, is smaller close to the free surface (Figures 17g, 17h and 17j). Such profiles are often observed in granular flows [see e.g. *GDR Midi*, 2004; *Lajeunesse et al.*, 2005; *Siavoshi and Kudrolli*, 2005; *Lube et al.*, 2007; *Forterre and Pouliquen*, 2008; *Mangeney et al.*, 2010]. The velocities within the flow and the erodible bed increase with increasing front velocity V_f. The surface of the erodible bed is entrained to the maximum velocity of 118 mm s^{-1} when V_f is maximum ($\simeq 180$ cm s^{-1}, Figures 17a and 17h). At the end of the slow propagation phase ($V_f < 50$ cm s^{-1}), there is almost no excavation at the upper surface of the erodible bed (Figures 17a and 17k).

For all experimental combinations, the bed is generally excavated deeper and for a longer time as the bed thickness h_i increases until $h_i \simeq 7d$ to $14d$ (Figures 18a to 18d). For thicknesses h_i greater than $21d$, the maximum depth h_C and the duration t_d of excavation are generally both smaller than for $h_i < 21d$, except for $\theta = 22°$, $a = 1.24$ and $V = 5600$ cm^3 (Figures 18a to 18d). The maximum depth h_C and duration t_d of excavation generally increase as the slope angle θ increases and as bed compaction decreases (Figure 19) but are systematically smaller for release from the trapezoidal reservoir than for release from the rectangular reservoir and when the channel is narrow (10-cm-wide) (Figures 18b and 18d). The maximum value of $h_C(h_i)$ globally increases with a (Figure 19a) and V (Figure 19b) and more generally with the initial height h_0, which controls the maximum front velocity (Figure 7d). The maximum value of $t_d(h_i)$ increases with the volume V (for $a = 0.7$) and even more so when the slope angle θ increases (Figure 19d). We did not notice any significant variation of the excavation duration with aspect ratio a (Figure 19c). As a result, the increase in runout distance over the erodible bed compared to that over the rigid bed Δr_f increases with the duration of bed excavation t_d (Figure 18e). In contrast, no relation between runout distance and maximum excavation depth h_C was observed.

5.5. Erosion Waves

Waves made of particles excavated from the erodible bed at the flow head were observed for flows over erodible beds [*Mangeney et al.*, 2010; *Rowley et al.*, 2011]. It is not however clear how the characteristics of these waves affect erosion efficiency. These waves were studied mainly at slope angles $\theta \geq 22°$ where bed erosion is significant (Figure 20). At lower slope angles, their amplitude was too small to be captured. The waves propagate downstream, develop to their maximum amplitude A and then disappear rapidly (Figures 20b to 20h). For $\theta = 24.5°$, $V = 12600$ cm^3 and $a = 0.7$, when the front velocity is maximum, the waves reached a maximum amplitude of 10 to 12 particle diameters (i.e. 0.7 ± 0.2 cm to 0.8 ± 0.2 cm) and a maximum velocity of 85 ± 10 cm s^{-1}, about 3 times smaller than the front velocity at the same position (Figures 20c to 20h; see also the video in the auxiliary material). Upstream of the flow front, the wavelength increases and the amplitude decreases [e.g. *Mangeney et al.*, 2010; *Rowley et al.*, 2011]. The erosion waves disappear as the front decelerates and are not visible in the final deposit: the interface between the flow and the bed is a relatively thin but uniform mix of flow and substrate particles (Figure 20i).

Interestingly, the maximum amplitude A and duration t_{waves} of the waves varied similarly with a and V to the maximum depth h_C and duration t_d of excavation, respectively (Figures 19, 20j and 20k). The maximum amplitude of the erosion waves increased with a and V (Figure 20j). For $a = 0.7$ and $V = 1400$ cm^3, a wave barely emerged behind the flow front and reached 3 particle diameters of amplitude above the erodible bed. At the position from the gate where waves reached their maximum amplitude, the wave duration t_{waves} increased with the volume V but did not significantly increase with aspect ratio a (Figure 20k). In all the experiments, t_{waves} was less than 10% of the flow duration.

At the free surface of the flow, other waves were also observed above the subjacent "black" waves (Figures 20b to 20h). Such instabilities also appeared at the free surface of flows over a rigid bed (i.e. for $h_i = 0$ mm), but were of lower amplitude than those observed for flows on an erodible bed. Such surface waves may be explained by small irregularities in the roughness of the channel base.

6. Discussion

6.1. Critical Slope Angle and Different Flow Regimes

We have quantified the influence of several initial and boundary conditions on the dynamics and deposition processes of granular flows over slope angles smaller than the friction angle of the material involved. The flow dynamics change when the slope angle exceeds a critical value θ_c between 10° to 16°, both over rigid and erodible beds. Regardless of the experimental combinations, this critical angle is more or less the same, i.e. about half the repose angle of the material.

When $\theta < \theta_c$, the flow front deceleration lasts as long as the acceleration phase (Figures 7c, 8a and 8b). The deposit front has a flat, low angle termination (Figures 6a to 6c). The maximum velocity is scaled by $\sqrt{gh_0 \cos\theta}$ (Figure 7d) and the well established scaling law (6) relating the runout distance r_f to the initial column height h_0 is satisfied (Figures 4a and 4b). This is characteristic of the spreading phase observed for granular collapse over horizontal beds. In this regime (i.e. $\theta < \theta_c$), the runout distance is not affected by the presence of an erodible bed (Figure 9). Only the profile of the deposit changes slightly (Figure 14c).

On the other hand, when the slope angle θ exceeds the critical angle θ_c, a final regime of slow propagation develops

after the deceleration phase (Figures 7a to 7c). In that case, the scaling laws (e.g. equation (6)) derived from granular collapse experiments over horizontal planes are no longer valid: the normalized runout distance r_f/r_0 depends both on the aspect ratio a and on the volume V (Figures 3b and 3c). This has never before been reported. The characteristics of the slow propagation phase are similar to those of steady uniform flows [*Pouliquen*, 1999a]: a steep front (Figures 6d to 6f, 14a and 14b), a slow and quasi-uniform velocity ($V_f < 50$ cm s^{-1}, Figures 7a to 7c, 15a, 15b and 15e) and a quasi-uniform thickness along the plane ($h \simeq 1$ to 2 cm, Figures 5 and 13). Furthermore, when the slow propagation phase is well developed and lasts longer than 1 s, the mean velocity of this slow phase and the mean thickness of the flow behind the front roughly satisfy the *Pouliquen* [1999a] flow law (7) (Figure 16a). This slow propagation phase tending to steady uniform flow is observed at slope angles smaller than the minimum angle for which steady uniform flows are observed, $\theta_1 = 24.4°$, when using the classical method for generating these flows (i.e. a constant supply upstream, Figures 1a and 2). The initial and boundary conditions that lead to this slow propagation phase at slope angles smaller than θ_1 provide additional energy to the system making it possible to compensate the energy lost by friction. The deposit of these quasi-uniform flows is almost parallel to the plane (Figures 5 and 13) as observed for steady-uniform flows when the supply is cut. Interestingly, if we plot the maximum value of the thickness of this deposit (Figures 16b and 16c), it follows a curve close to that of $h_s(\theta)$, obtained after steady uniform flows (Figure 2). This suggests that the initial and boundary conditions can significantly expand the parameter space where steady uniform flows can develop. Furthermore, it suggests that the friction law proposed by *Pouliquen* [1999a]:

$$\mu(u,h) = \mu_1 + (\mu_2 - \mu_1)\exp(-\frac{h_s}{Ld}) \qquad (8)$$

could be extended to smaller slopes where it would involve smaller values of the friction coefficient μ_1 because $\mu_1 = \tan\theta_1$. In equation (8), $\mu_1 = \tan\theta_1$ and $\mu_2 = \tan\theta_2$ are the friction coefficients that correspond respectively to the minimum and maximum slope angles θ_1 and θ_2 for which steady uniform flows are observed and L is a characteristic dimensionless thickness [*Pouliquen*, 1999a]. This could have a strong implication for natural flows where very large volumes can be involved that may significantly decrease μ_1. Note that very small effective friction is observed in natural flows, especially for large volumes [*Pirulli and Mangeney*, 2008; *Lucas et al.*, 2011; *Mangeney et al.*, 2012].

6.2. Crucial Role of the Duration of the Slow Propagation Phase

Several initial and boundary conditions contribute to initiate or increase the duration of the slow propagation phase (i.e. the quasi-uniform flows) by adding energy to the system to overcome friction. This additional energy can come from: (i) increasing the slope angle which increases the driving force due to gravity; (ii) increasing the volume at constant aspect ratio or decreasing the aspect ratio at a constant volume because the supply is maintained longer at a roughly constant rate due to the relatively longer reservoir; (iii) entrainment of material from the erodible bed that increases the kinetic energy of the flowing mass [*Mangeney et al.*, 2007a]; (iv) enlarging the channel width which reduces the effective friction due to the walls [*Jop et al.*, 2005]; or (v) increasing the angle of the gate inclination with respect to the slope that gives a higher initial driving force due to the pressure gradient [see equation (2) of *Mangeney-Castelnau et al.*, 2003]. Note that the influence of the aspect ratio is less obvious than that of the volume (Figures 9c, 15f, 19a and 19c). In our experiments, the range of aspect ratios investigated may not be large enough to observe a significant variation of the dynamics, as opposed to the volume range. We however chose to use small values of aspect ratio ($a \leq 1.24$) to be consistent with many geophysical flows.

The increase in the runout distance over an erodible bed compared to that over a rigid bed occurs during the deceleration phase or during the slow propagation phase (Figures 15c and 15d). The percentage of the increase as a function of the rigid bed runout distance varies depending on the initial conditions (Figures 9e and 9f). As these two regimes are fundamentally different, varying the experimental conditions will affect their respective duration in a different way over rigid and erodible beds. For example, increasing the aspect ratio increases the duration of the deceleration phase but the slow propagation phase lasts longer for smaller aspect ratios (e.g. Figure 7a). It is therefore difficult to interpret the variation of the increase in the runout distance in percentage of the runout distance over the rigid bed for different initial conditions (Figures 9e and 9f). It is clear, however, that the increase of runout distance increases with the slow phase duration over an erodible bed (for $\theta = 22°$, compare Figures 9c and 9d and Figures 15f and 15g). As a result the duration of the slow propagation phase seems to play a key role in the efficiency of erosion processes.

6.3. Erosion Processes and Runout Distance

The durations of excavation of the erodible bed and of the erosion waves increase with the duration of the slow propagation phase (compare Figures 15f and 15g and Figures 19c, 19d and 20k). On the other hand, the maximum depth of excavation is not affected by the duration of the slow propagation phase. Instead, the depth of excavation appears to be controlled by the maximum front velocity because both increase with the initial column height and slope angle (Figures 7d, 19a and 19b). Initial column shape has a variable effect on excavation depth: although the maximum front velocity for a similar volume and slope angle is the same for both the trapezoidal and rectangular column shapes, the excavation depth is smaller for the trapezoidal column (Figures 15e and 18b).

As a result, the capacity of a flow to increase its runout distance over an erodible bed does not depend on the maximum excavation depth. For instance, the bed is more deeply excavated during acceleration (Figure 17b) but this phase does not contribute to the runout distance increase (Figures 15c and 15d). During flow initiation and the acceleration phase, the granular flow is driven mainly by a longitudinal thickness gradient that tends to push the mass down the slope, as reported by *Mangeney-Castelnau et al.* [2003]. At the beginning of the collapse, thickness gradients are only slightly affected by the presence of an erodible bed, which is much thinner than the flow. The acceleration phase and maximum front velocity are consequently little affected either (Figures 7, 15a, 15b and 15e), although a large amount of bed erosion occurs during this phase.

An important feature of granular collapse dynamics is the transition from vertical fall to slope-parallel movement. At the beginning, a significant portion of the potential energy is transformed into kinetic energy corresponding to motion in a direction perpendicular to the slope while later on almost all the kinetic energy is related to motion in the downslope direction. For flows over an erodible bed, when the front is accelerating, the kinetic energy of motion in the direction perpendicular to the slope is absorbed by the bed. The erodible bed is therefore affected deeply but for a very short time (Figure 17b). On the other hand, as the flow front decelerates, if most of the flow kinetic energy is related to motion in the downslope direction, the grains from the erodible

bed that are put into motion will more easily join the flow. Furthermore, during the deceleration and slow propagation phases, even if the bed is excavated to a shallower depth, the excavation occurs over a longer time (Figures 17c to 17e). Therefore, the increase in the runout distance compared to that over the rigid bed depends on the ability of the flow to transfer its energy to the erodible bed through motion in the direction of propagation over a long time and consequently over a large distance.

Depending on the initial geometry and volume of the column, the energy in the system will be dissipated differently. For example, for $\theta = 22^\circ$ and a given volume $V = 5600$ cm^3, the runout distance of a flow of relatively high initial aspect ratio ($a = 1.24$) is not considerably higher over an erodible bed than over a rigid bed and may even be smaller in certain cases (Figure 10a). This lack of difference in runout distance occurs because the flow loses the majority of its vertical-motion kinetic energy by reworking the bed in the direction perpendicular to the slope rather than in the propagation direction. For this specific case, the resulting kinetic energy of motion in the direction of propagation is significantly reduced during the deceleration phase and the front therefore moves slower over an erodible bed than over a rigid bed (Figure 15c). In contrast, a flow with a small initial aspect ratio excavates more of the bed in the propagation direction than in the direction perpendicular to the slope (when the aspect ratio decreases the excavation depth is smaller but not the excavation duration, Figures 19a and 19c). For a given aspect ratio ($a = 0.7$), when the volume increases, the flow loses more perpendicular-motion kinetic energy to deeper bed excavation (Figure 19b). However, the volume increase also promotes a longer duration of the slow propagation phase owing to the increase in the mass supply (Figure 15g). Hence, the increase in the runout distance is greater for higher volumes (Figures 9d).

6.4. Influence of Bed Compaction and Channel Width on Runout Distance and Erosion

The degree of bed compaction has an influence on the dynamics of granular flows and on the efficiency of the erosion processes, especially for slope angles close to the repose angle of the granular material (typically $\theta = 22^\circ$). In general, more energy is needed to remove particles from a more compact erodible bed than from a loosely-packed substrate. As a consequence, the more compact bed is excavated over a shallower depth and for a shorter time (Figure 19) and the runout distance over it is smaller (Figure 10).

For granular flows in a channel, the horizontal velocity profile perpendicular to the flow direction resembles a so-called Couette profile since the side of the flow is slowed by sidewall friction [*GDR Midi*, 2004; *Jop et al.*, 2005]. Because the excavation depth appears to be related to the front velocity, it is assumed to be greater in the middle of the channel than along the sidewalls. Hence, when measuring internal features and velocity profiles on one side of the flow (through the transparent channel wall), one must be aware that they may be not representative of those in the middle of the channel. Observations by *Rowley et al.* [2011] support this assumption. In their experiments on granular flows over an erodible bed, the waves preserved in the deposits are developed to a far greater extent away from the sidewalls.

Over the rigid bed, runout distances are about 10% smaller in a narrow (10-cm-wide) channel than in a wider (20-cm-wide) channel for experiments with slope angles $\theta = 0^\circ$ and $\theta = 10^\circ$ and about 20% smaller for $\theta = 22^\circ$ (Figures 4c). For flows over an erodible bed, the increase in the runout distance is smaller when the channel width is narrow. At $\theta = 22^\circ$, a 30% deviation is observed in the runout distance and a 10% deviation is reported in maximum erosion depth between the narrow and wider channels (Figures 9b and 18b). Indeed, as illustrated in Figure 2, $h_s(\theta)$ is larger for $W = 10$ cm than for $W = 20$ cm, so that a layer of a given thickness h_i is more stable for $W = 10$ cm than for $W = 20$ cm, making it harder to put the grains in motion. As a consequence, our results are dependent on channel width. In channelized experiments of column collapse onto a horizontal plane, *Balmforth and Kerswell* [2005] and *Lacaze et al.* [2008] also showed that runout distance varies with channel width. Therefore, the channel width should be considered in numerical models of confined 2D flows [e.g. *Lacaze et al.*, 2008].

6.5. Erosion Waves

The presence of waves in the flow head suggests that a significant portion of the energy exchanges between the flow and the underlying bed takes place within this zone (Figures 20b to 20h). However, the influence of these waves on the erosion efficiency remains unclear.

The waves observed at the bed interface may be compared to a Kelvin-Helmholtz instability, where two fluids of different velocities and densities are superimposed. The erodible bed is an initially static and compacted granular medium whereas the avalanche is a relatively less dense moving mass. Assuming that these two layers can be considered as two fluids, the Kelvin-Helmholtz conditions are fulfilled. In fluids, a small perturbation at the interface is amplified by the local velocity difference and a corresponding local decrease of the flow pressure. If the velocity of the superjacent fluid is sufficient, the amplified perturbation transforms into a breaking wave. *Rowley et al.* [2011] developed a criterion that gives the minimum velocity difference $v_1 - v_2$ between the upper (1) and lower (2) layers for a given wavelength λ and granular concentrations Φ_1 and Φ_2 for the growth of so-called Kelvin-Helmholtz instabilities:

$$v_1 - v_2 \geq \sqrt{\frac{g\lambda}{2\pi}\left(\frac{\Phi_2}{\Phi_1} - \frac{\Phi_1}{\Phi_2}\right)} \tag{9}$$

where g is acceleration due to gravity. In our specific case, for $\theta = 22^\circ$, $V = 12600$ cm^3 and $a = 0.7$ (Figures 20a to 20i), the wavelength λ is about 7 cm. In dense granular flows such as those studied here, the flow bulk density does not change significantly over the flow thickness [see e.g. *GDR Midi*, 2004]. Taking $\Phi_1 \simeq 6400$ grains per cm^3 $\simeq 0.8\Phi_2$, we have $\Phi_2/\Phi_1 - \Phi_1/\Phi_2 < 1$. Thus $\sqrt{\frac{g\lambda}{2\pi}(\Phi_2/\Phi_1 - \Phi_1/\Phi_2)} \leq 0.4$ m s^{-1}. For a velocity difference equal to the maximum front velocity, $v_1 - v_2 \simeq 2$ m s^{-1}. Therefore, according to the growth criterion (9), Kelvin-Helmholtz instabilities may have developed in our experiments. The analogy with Kelvin-Helmholtz, however, is not straightforward because a well-developed instability requires a velocity difference to be maintained between the two fluids. In our experiments, the velocity difference is sufficiently high only at the flow head. The waves are consequently observed only in the flow head and only when the front velocity exceeds 0.4 m s^{-1} (Figures 20b to 20h). Note, however, that we observed an increase in wave amplitude with front velocity as slope angle and column aspect ratio and volume increased (Figure 20j).

In experiments on dense granular flows moving over an erodible bed, *Rowley et al.* [2011] and *Dufresne* [2012] also observed waves in the bed that were generated by entrainment of the substrate. In both these studies, the waves were preserved in the deposits unlike in our experiments where the erosion waves disappeared as the flow front decelerated (Figure 20i). As their experimental setup ends on a subhorizontal surface, the flow may stop rapidly which could freeze the waves within the deposit. Thus, if such waves exist in natural gravitational flows at the substrate interface, they may or may not be visible in natural deposits.

7. Conclusions

We carried out experiments on dry granular flows generated by column collapse onto an inclined channel, both over a rigid and an erodible bed. For several slope angles ranging from 0° to 24°, we varied the initial conditions (column aspect ratio, volume and shape) and the boundary conditions (presence of an erodible bed, bed thickness and degree of compaction, channel width) systematically to quantify the changes in granular flow dynamics and deposition processes for increasing slope angles. A number of conclusions can be drawn from our results.

1. For slope angles below a critical angle θ_c, runout distances of flows over a rigid bed match scaling laws previously proposed in the literature: runout distance depends only on the initial column height. In contrast, those scaling laws are no longer valid when the slope angle is increased beyond θ_c. This seems to be related to the development of a slow propagation phase for $\theta > \theta_c$, tending to quasi-steady uniform flows with characteristics similar to those observed at higher slopes by *Pouliquen* [1999a].

2. For flows over an erodible bed, the runout distance increases by up to about 50% compared to that over a rigid bed when the slope angle is greater than θ_c. When the bed thickness is increased, the runout distance increases linearly or first increases and tends towards a maximum before ultimately decreasing, depending on the degree of bed compaction. Furthermore, the runout distance increase is greater and the bed excavation is deeper and lasts longer as bed compaction decreases.

3. Bed excavation is not uniform along the flow propagation and depends on flow front velocity. As the flow accelerates, the erodible bed is deeply excavated but only very briefly. In contrast, as the flow decelerates, bed excavation is shallower but lasts longer. The increase in runout distance over an erodible bed is greater when the duration of bed excavation increases, but no relation was found with the maximum excavation depth.

4. The increase in the runout distance caused by an erodible bed is not due only to an increase in the flowing mass by bed entrainment. It is clearly also related to the development of a slow propagation phase after front deceleration for slope angles greater than θ_c. The duration of the slow propagation phase has a crucial impact on flow dynamics and deposition: as the duration of the slow propagation phase increases, bed excavation lasts longer and the flow propagates further.

5. The following parameters were shown to increase the duration of the slow propagation phase: (i) increasing slope angle, column volume, inclination of the column with respect to the slope and channel width; (ii) diminishing column aspect ratio; and (iii) addition of an erodible bed. The duration of the slow propagation phase is, however, independent of the maximum flow front velocity and, for flows over an erodible bed, of the maximum depth of excavation within the bed.

Further work is required to investigate the link between erosion/deposition efficiency and the properties of the granular material, including cohesion, shape, size of the grains, etc. Although the configuration studied here is very simple, our experimental results provide a new and better understanding of the processes that control the dynamics and deposition of geophysical granular flows. A major challenge for numerical models is to take these parameters into account and reproduce the complex phenomena at the interface between the flow and the substrate. Our results provide quantitative data that can be used to constrain such models. Some of the data, such as runout distance and excavation depth, are, however, biased by the sidewall effects in our experimental setup. Therefore, further investigations and numerical simulations should focus on unconstrained 3D granular flows.

Acknowledgments. We are grateful to Andrew Hogg for providing us with his experimental results. We thank Olivier Pouliquen for suggesting the experiments to test the potential effect of the addition of mass to the flow caused by bed erosion. We are indebted to Eliza Calder, Patrick Richard and Paul D. Cole, Paddy Smith and Adam Stinton from the MVO, Montserrat, Lesser Antilles for fruitful discussions. We are grateful to Jon Major and three anonymous reviewers for their interesting comments. This work was supported by the Agence Nationale de la Recherche ANR UNDERVOLC, ANR LANDQUAKES and ANR VOLBIFLO. It is IPGP contribution n°3454 and Laboratory of Excellence ClerVolc contribution n° 80.

References

Berger, C., B.W. McArdell, and F. Schlunegger (2011). Direct measurement of channel erosion by debris flows, Illgraben, Switzerland. J. Geophys. Res. 116, F01002, doi:10.1029/2010JF001722.

Balmforth, N. and R. Kerswell (2005). Granular collapse in two dimensions. J. Fluid Mech. 538, 399-428.

Bernard, K. and B. Van Wyk de Vries (2011). Characterization of breccia structure at the base of large landslides: a necessary step for modeling. European Geophysical Union meeting, Vienna. EGU2011-6310.

Bouchut, F., A. Mangeney-Castelnau, B. Perthame, and J.P. Vilotte (2003). A new model of Saint-Venant and Savage-Hutter type for gravity driven shallow water flows, C. R. Acad. Sci. Paris Ser. I, 336, 531-536.

Bouchut, F. and M. Westdickenberg (2004). Gravity driven shallow water models for arbitrary topography. Comm. in Math. Sci. 2(3), 359-389.

Bouchut, F., E. Fernandez-Nieto, A. Mangeney, and P. Y. Lagree (2008). On new erosion models of Savage-Hutter type for avalanches. Acta Mech., 199(1-4), 198-208.

Conway, S. J., A. Decaulne, M.R. Balme, J.B. Murray, and M.C. Towner (2010). A new approach to estimating hazard posed by debris flows in the Westfjords of Iceland, Geomorphology, 114, 556-572.

Crosta, G. B., S. Imposimato, and D. Roddeman (2009a). Numerical modeling entrainment/deposition in rock and debris avalanches, Eng. Geol., 109, 135-145.

Crosta, G. B., S. Imposimato, and D. Roddeman (2009b). Numerical modeling of 2-D granular step collapse on erodible and nonerodible surface, J. Geophys. Res., 114, F03020, doi:10.1029/2008JF001186.

Denlinger, R. P., and R. M. Iverson (2001). Flow of variably fluidized granular masses across three-dimensional terrain: 2. Numerical predictions and experimental tests, J. Geophys. Res., 106, 553-566, doi:10.1029/2000JB900330.

Denlinger, R. P., and R. M. Iverson (2004). Granular avalanches across irregular three-dimensional terrain: 1. Theory and Computation, J. Geophys. Res., 109, F01014, doi:10.1029/2003JF000085.

Dufresne, A. (2012). Granular flow experiments on the interaction with stationary runout path materials and comparison to rock avalanche events, Earth Surf. Process. Landforms 37, 1527-1541.

Estep, J. and J. Dufek (2012). Substrate effects from force chain dynamics in dense granular flows. J. Geophys. Res., 117, F01028, doi:10.1029/2011JF002125.

Favreau, P., A. Mangeney, A. Lucas, G. Crosta, and F. Bouchut (2010). Numerical modeling of landquakes. Geophys. Res. Lett., 37, L15305, doi:10.1029/2010GL043512.

Forterre, Y. and O. Pouliquen (2008). Flows of dense granular media. Annu. Rev. Fluid Mech., 40, 1-24.

G. D. R. Midi (2004). On dense granular flows. Eur. Phys. J. E. 14, 4, 341-365.

Hogg, A. (2007). Two-dimensional granular slumps down slopes. Phys. Fluids. 19, 093301, doi: 10.1063/1.2762254

Hungr, O., and S. G. Evans (2004). Entrainment of debris in rock avalanches: An analysis of a long run-out mechanism. Bull. Geol. Soc. Am., 116, 1240-1252.

Iverson, R. M., M. Reid, M. Logan, R. LaHusen, J. W. Godt and J. Griswold (2011). Positive feedback and momentum growth during debris-flow entrainment of wet bed sediment. Nature Geoscience 4, 116-121, doi: 10.1038/NGEO1040.

Iverson, R. M. (2012). Elementary theory of bed-sediment entrainment by debris flows and avalanches. J. Geophys. Res., 117, F03006, doi:10.1029/2011JF002189.

Jop, P., Y. Forterre, and O. Pouliquen (2005). Crucial role of side walls for granular surface flow: consequences for the rheology. J. Fluid Mech. 541, 167-192

Kerswell, R. (2005). Dam break with coulomb friction: A model of granular slumping ? Phys. Fluids. 17, 057101, doi:10.1063/1.1870592.

Lacaze, L., J. Phillips, and R. Kerswell (2008). Planar collapse of a granular column: experiments and discrete element simulations. Phys. Fluids 20, 063302.

Lajeunesse, E., A. Mangeney-Castelnau, and J. P. Vilotte (2004). Spreading of a granular mass on a horizontal plane, Phys. Fluids, 16, 2371-2381.

Lajeunesse, E., J. Monnier, and G. Homsy (2005). Granular slumping on a horizontal surface. Phys. Fluids 17, 103302, doi: 10.1063/1.2087687.

Lube, G., H. E. Huppert, R. S. J. Sparks, and M. A. Hallworth (2004). Axisymmetric collapses of granular columns. J. Fluid Mech, 508, 175-199.

Lube, G., H. E. Huppert, R. Sparks, and A. Freundt (2005). Collapses of two-dimensional granular columns. Physical Review E72, 041301, doi:10.1103/PhysRevE.72.041301.

Lube, G., H. E. Huppert, R. Sparks, and A. Freundt (2007). Static and flowing regions in granular collapses down channels. Phys. Fluids. 19, 043301, doi: 10.1063/1.2712431.

Lube, G., H. E. Huppert, R. Sparks, and A. Freundt (2011). Granular column collapses down rough, inclined channels. J. Fluid Mech. 675, 347-368.

Lucas, A., A. Mangeney, D. Mège, and F. Bouchut (2011). Influence of Scar Geometry on landslide dynamics and deposits: Application to Martian landslides. J. Geophys. Res.- Planets, 116, E10001, doi: 10.1029/2011JE003803.

Mangeney, A., P. Heinrich, and R. Roche (2000). Analytical solution for testing debris avalanche numerical models. Pure Appl. Geophys., 157, 1081-1096.

Mangeney-Castelnau, A., J. P. Vilotte, M. O. Bristeau, B. Perthame, F. Bouchut, C. Simeoni, and S. Yernini (2003). Numerical modeling of avalanches based on Saint-Venant equations using a kinetic scheme. J. Geophys. Res., 108 (B11), 2527. doi: 10.1029/2002JB002024.

Mangeney-Castelnau, A., F. Bouchut, J. P. Vilotte, E. Lajeunesse, A. Aubertin, and M. Pirulli (2005). On the use of Saint Venant equations to simulate the spreading of a granular mass. J. Geophys. Res. 110., B09103, doi:10.1029/2004JB003161.

Mangeney, A., L. S. Tsimring, D. Volfson, I. S. Aranson, and F. Bouchut (2007a). Avalanche mobility induced by the presence of an erodible bed and associated entrainment. Geophys. Res. Lett., 34, L22401, doi:10.1029/2007GL031348.

Mangeney, A., F. Bouchut, N. Thomas, J. P. Vilotte, and M. O. Bristeau (2007b). Numerical modeling of self-channeling granular flows and of their levee-channel deposits. J. Geophys. Res., 112, F02017, doi:10.1029/2006JF000469.

Mangeney, A., O. Roche, O. Hungr, N. Mangold, G. Faccanoni, and A. Lucas (2010). Erosion and mobility in granular collapse over sloping beds, J. Geophys. Res., 115, F03040, doi:10.1029/2009JF001462.

Mangeney, A., A. Lucas, and J.P. Ampuero (2012). Volume dependence of landslide effective friction on Earth and beyond, Abstract EP13B-0839 presented at 2012 Fall Meeting, AGU, San Francisco, Calif., 3-7 Dec.

McCoy, S.W., G.E. Tucker, J.W. Kean, and J.A. Coe (2013). Field measurement of basal forces generated by erosive debris flows. J. Geophys. Res., 118(2), 589-602.

Moretti, L., A. Mangeney, Y. Capdeville, E. Stutzmann, C. Huggel, D. Schneider, and F. Bouchut (2012). Numerical modeling of the Mount Steller landslide flow history and of the generated long period seismic waves. Geophys. Res. Lett. 39, L16402, doi:10.1029/2012GL052511

Pirulli, M., and Mangeney, A. (2008). Result of back-analysis of the propagation of rock avalanches as a function of the assumed rheology. Rock Mech. Rock Eng. 41(1), 59-84.

Pouliquen, O. (1999a). Scaling laws in granular flows down rough inclined planes. Phys. Fluids 11(3), 542-548.

Pouliquen, O. and Y. Forterre (2002). Friction law for dense granular flows: application to the motion of a mass down a rough inclined plane. J. Fluid Mech. 453, 133-151.

Roche, O., S. Montserrat, Y. Niño, and A. Tamburrino (2008). Experimental observations of water-like behavior of initially fluidized, unsteady dense granular flows and their relevance for the propagation of pyroclastic flows. J. Geophys. Res. 113, B12203, doi: 10.1029/2008JB005664.

Roche, O., M. Atalli, A. Mangeney, and A. Lucas (2011). On the run-out distance of geophysical gravitational flows: insight from fluidized granular collapse experiments. Earth and Planetary Science Letters 311, 375-385, doi: 10.1016/j.epsl.2011.09.023.

Roche, O., Y. Niño, A. Mangeney, B. Brand, N. Pollock, and G.A. Valentine (2013). Dynamic pore-pressure variations induce substrate erosion by pyroclastic flows. Geology 41, doi: 10.1130/G34668.1.

Rowley, P. J., P. Kokelaar, M. Menzies, and D. Waltham (2011). Shear-derived mixing in dense granular flows. J. Sed. Res. 81, 874-884.

Savage, S. B. and K. Hutter (1989). The motion of a finite mass of granular material down a rough incline. J. Fluid Mech. 199, 177-215.

Schürch, P., A.L. Densmore, N.J. Rosser, and B.W. McArdell (2011). Dynamic controls on erosion and deposition on debris-flow fans. Geology 39, 827-830.

Siavoshi, S. and A. Kudrolli (2005). Failure of a granular step. Phys. Rev E. 71, 051302.

Sovilla, B., P. Burlando, and P. Bartelt (2006). Field experiments and numerical modeling of mass entrainment in snow avalanches. J. Geophys. Res. 111, F03007, doi:10.1029/2005JF000391.

Staron, L. and E. Hinch (2006). The spreading of a granular mass: role of grain properties and initial conditions. Granular Matter 9, 205-217, doi:10.1007/s10035-006-0033-z.

M. Farin, Institut de Physique du Globe de Paris, Equipe de Sismologie, 1 rue Jussieu, 75238 Paris cedex 05, PRES Sorbonne Paris Cité, France. (farin@ipgp.fr)

A. Mangeney, Université Paris-Diderot 7, Institut de Physique du Globe de Paris, Equipe de Sismologie, 1 rue Jussieu, 75238 Paris cedex 05, PRES Sorbonne Paris Cité, France. (mangeney@ipgp.fr)

O. Roche, Laboratoire Magmas et Volcans, Université Blaise Pascal - CNRS UMR6524 - IRD R163, 5 rue Kessler, F-63038 Clermont-Ferrand, France. (o.roche@opgc.univ-bpclermont.fr)

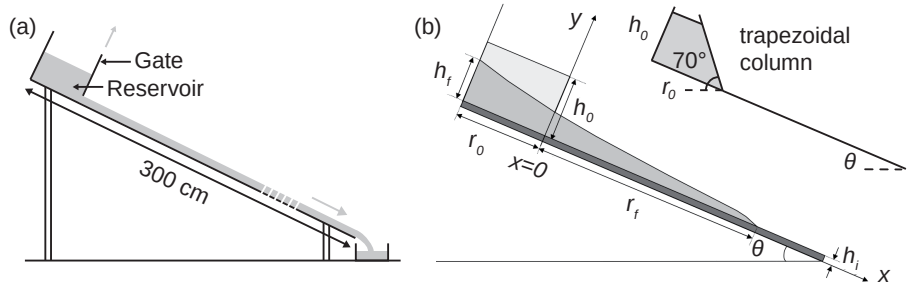

Figure 1. (a) Experimental design used to build an erodible bed over an inclined rough channel base (based on the *Pouliquen* [1999a] method for the study of steady uniform flows). (b) Morphometric and control parameters measured in the experiments and characteristics of a column with trapezoidal cross section. The initial granular column is contained in a reservoir of dimensions h_0 and r_0 (light gray). The erodible bed initially covering the rough channel base has a thickness h_i (dark gray). The deposit length r_f and final maximum height h_f (gray) were measured after each experiment [adapted from *Mangeney et al.*, 2010].

Table 1. Characteristics of the glass beads used in the experiments.

diameter d (μm)	density ρ_b (kg m^{-3})	repose angle θ_r (°)	avalanche angle θ_a (°)
600-800	2500	23±0.5	25±0.5

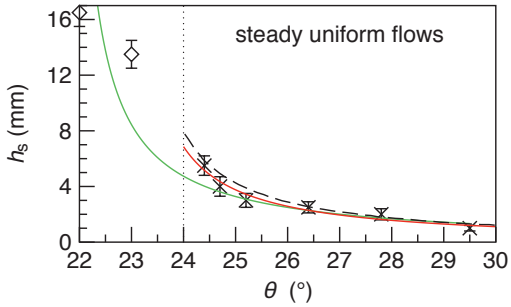

Figure 2. Thickness of the deposit h_s left on the rough base of inclination θ by a steady uniform flow after the mass supply from the reservoir has been cut (crosses, for $\theta > 24^\circ$). The maximum values of the mean thickness h_{dmean} of the deposits by the quasi-uniform flows from granular column collapses for $\theta = 22^\circ$ and $\theta = 23^\circ$ are also shown (empty diamonds, see Figures 16b and 16c and text in section 5.3.2). The red curve represents the best fit to the data for steady uniform flows and the green line is the best fit to all the data, using equation (1) proposed by *Mangeney et al.* [2010] for both fits. The black dashed line is the best fit to the data of *Mangeney et al.* [2010] with the 10-cm-wide channel.

Table 2. Characteristics of the different experiments[a]

Experiments	**E-W**	**E'-W**	**E^t-W**	**E22-K**	**E24-K**	**E-G**
Angle θ (°)	$0 \leq \theta \leq 24$	$0 \leq \theta \leq 22$	$0 \leq \theta \leq 24$	22	24.5	$0 \leq \theta \leq 24$
Aspect ratio a for $V = 5600$ cm^3	$0.3 \leq a \leq 1.24$	0.7	0.7	$0.45 \leq a \leq 1.24$	0.7	$0.3 \leq a \leq 1.24$
Volume V **(cm^3)** for $a = 0.7$	$1400 \leq V \leq 12600$	6300	12600	$1400 \leq V \leq 12600$	12600	$1400 \leq V \leq 12600$
Bed thickness h_i **(mm)**	$0 \leq h_i \leq 25$	$0 \leq h_i \leq 5$	$0 \leq h_i \leq 5$	7	4	$0 \leq h_i \leq 20$
Compaction method	*P, B, V*	*B*	*B*	*B*	*B*	*P, B, V*

[a] Experiments **E'** were carried out in a 10-cm-wide inclined channel. Experiments **E**^{t} were conducted with a trapezoidal column. The letters **W**, **K** and **G** indicate the type of beads used for the experiments: respectively white, black (colored) and gray (mixture of white and black beads). The last line shows the method used to create the erodible bed: *Pouliquen* [1999a] (P), board (B) or vibrated deposit (V) method.

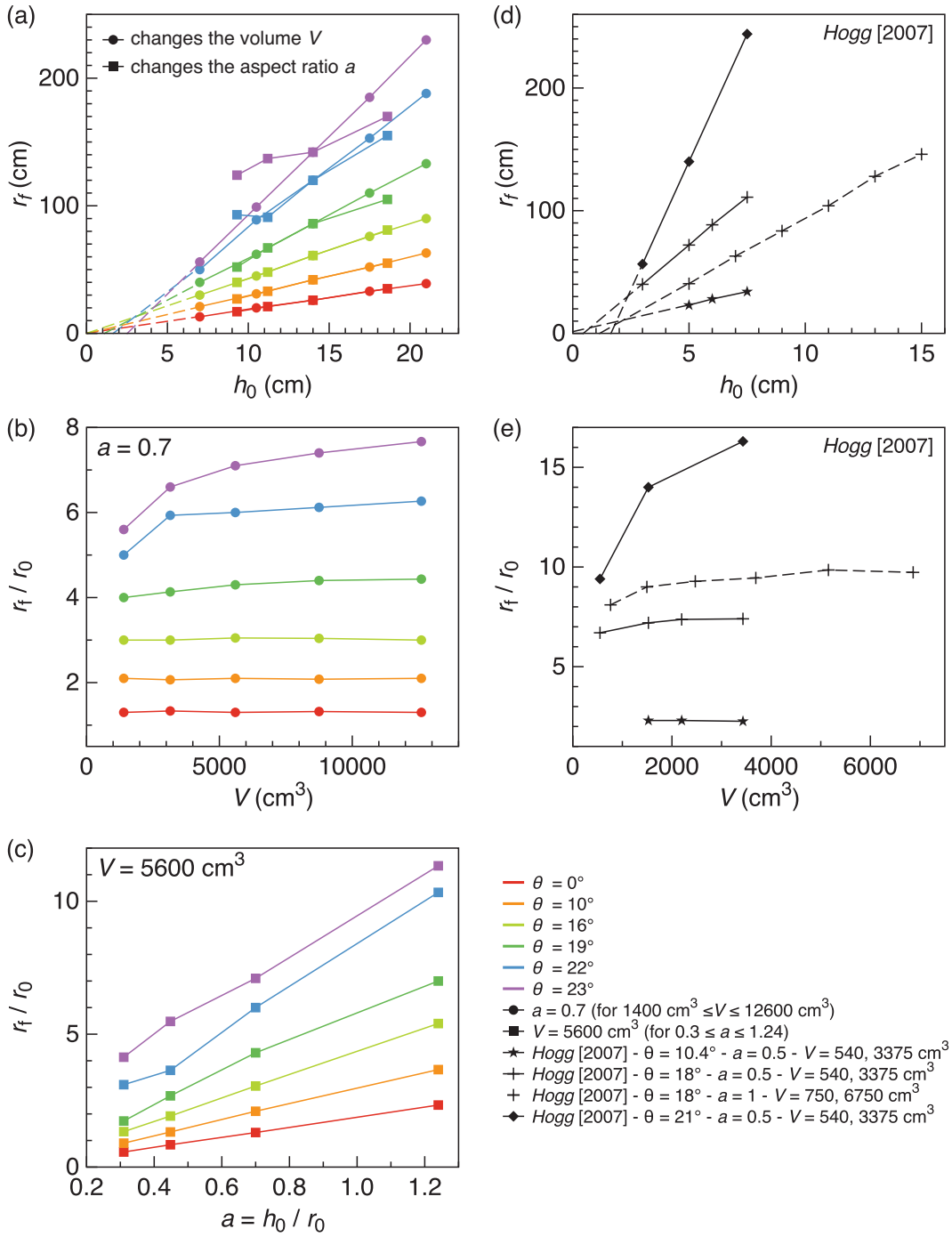

Figure 3. (a) Runout distance r_f as a function of the initial column height h_0 for $a = 0.7$ and different volumes V (circles), for $V = 5600$ cm^3 and different aspect ratios a (squares) and for different slope angles θ (colors) over the 20-cm-wide rigid bed. Normalized runout distance r_f/r_0 as a function of (b) the volume V for $a = 0.7$ and (c) the aspect ratio a for $V = 5600$ cm^3. (d) and (e) Results of *Hogg* [2007] for columns of Ballotini beads of diameter 100 μm released over a 30-cm-wide inclined rigid bed for various slope angles θ, a fixed aspect ratio $a = 0.5$ or $a = 1$ and different volumes V ranging from 540 cm^3 to 6750 cm^3. Error bars (not represented) are $\Delta(r_f) = \pm 2$ cm and $\Delta(r_f/r_0) = \pm 0.2$.

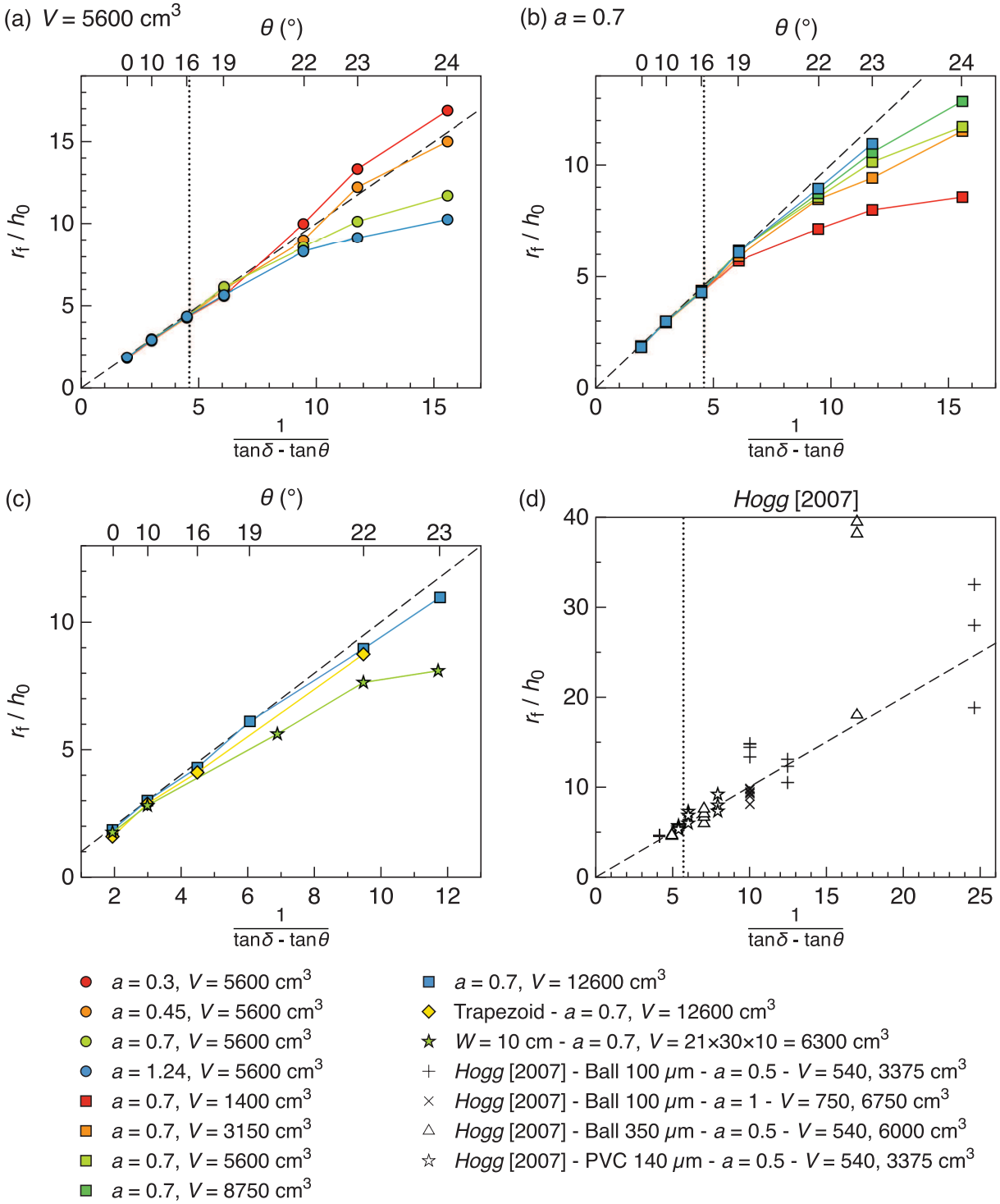

Figure 4. Normalized runout distance r_f/h_0 as a function of the slope angle θ and $1/(\tan\delta - \tan\theta)$ over the rigid bed of a 20-cm-wide channel for: (a) $V = 5600$ cm^3 and different aspect ratios a; (b) $a = 0.7$ and different volumes V. (c) Trapezoidal column collapse (diamond, $a = 0.7$ and $V = 12600$ cm^3) and flows in a 10-cm-wide channel (star, $h_0 = 21$ cm, $r_0 = 30$ cm, $a = 0.7$ and $V = 21 \times 30 \times 10 = 6300$ cm^3). Some results of *Hogg* [2007] are presented in (d) for column collapses of various volumes V ranging from 540 cm^3 to 6750 cm^3 and aspect ratios $a = 0.5$ and $a = 1$, over a 30-cm-wide inclined rigid bed with Ballotini beads of diameter 100 μm and 350 μm and PVC powder of diameter 140 μm. The black dashed line represents the theoretical trend (equation (6) with $k = 0.5$). The vertical dotted line represents an approximated position of the slope angle above which the scaling law (6) is no longer valid (see text). Error bars (not represented) are: $\Delta(1/(\tan\delta - \tan\theta)) = \pm 0.1$ and $\Delta(r_f/h_0) = \pm 0.2$.

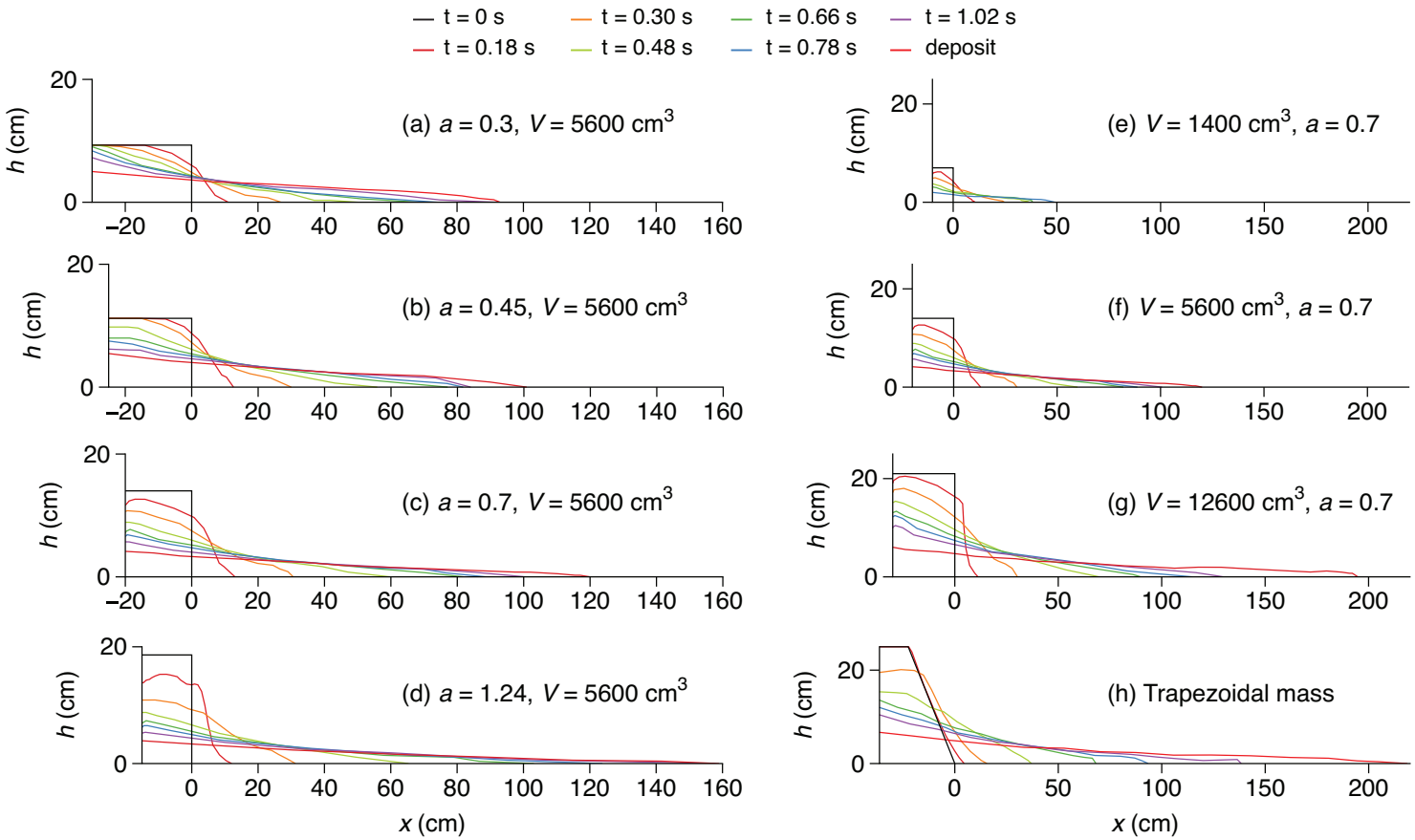

Figure 5. Different colored curves from top to bottom in each graph are thickness profiles $h(x,t)$ at different times t of the granular mass as a function of the downslope position x along the plane for flows over an inclined rigid bed with $\theta = 22^{\circ}$. (a)-(d) $V = 5600$ cm^3 and different aspect ratios a; (e)-(g) $a = 0.7$ and different volumes V and (h) a trapezoidal column with $V = 12600$ cm^3 and $a = 0.7$.

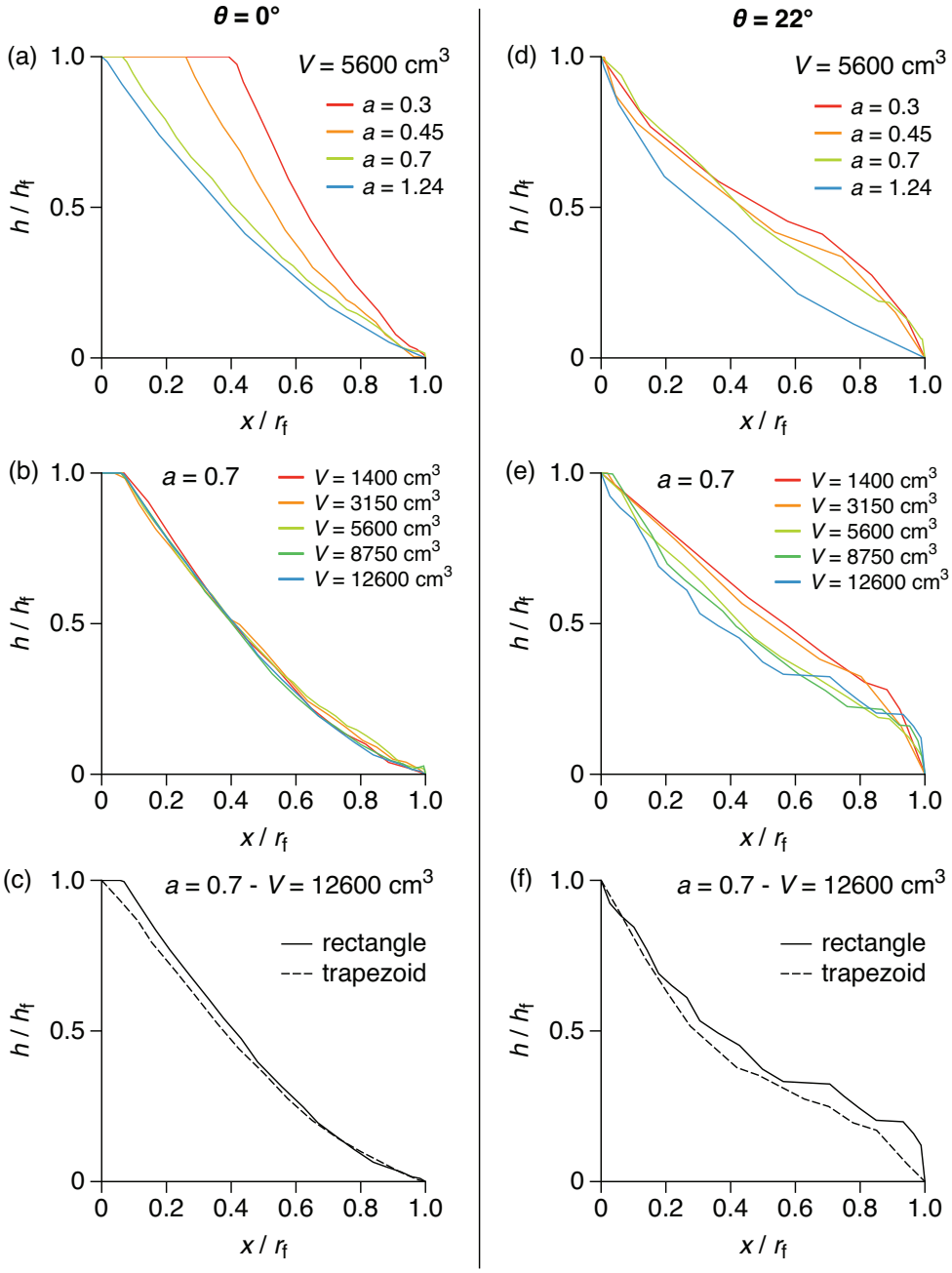

Figure 6. Final normalized thickness profile of the deposit h/h_f as a function of the normalized downslope position x/r_f over a rigid bed. The slope angle is $\theta = 0°$ for (a)-(c) and $\theta = 22°$ for (d)-(f). (a) and (d) are for $V = 5600$ cm^3 and different aspect ratios a. (b) and (e) are for $a = 0.7$ and different volumes V. (c) and (f) are for $a = 0.7$, $V = 12600$ cm^3 and the rectangular and trapezoidal columns.

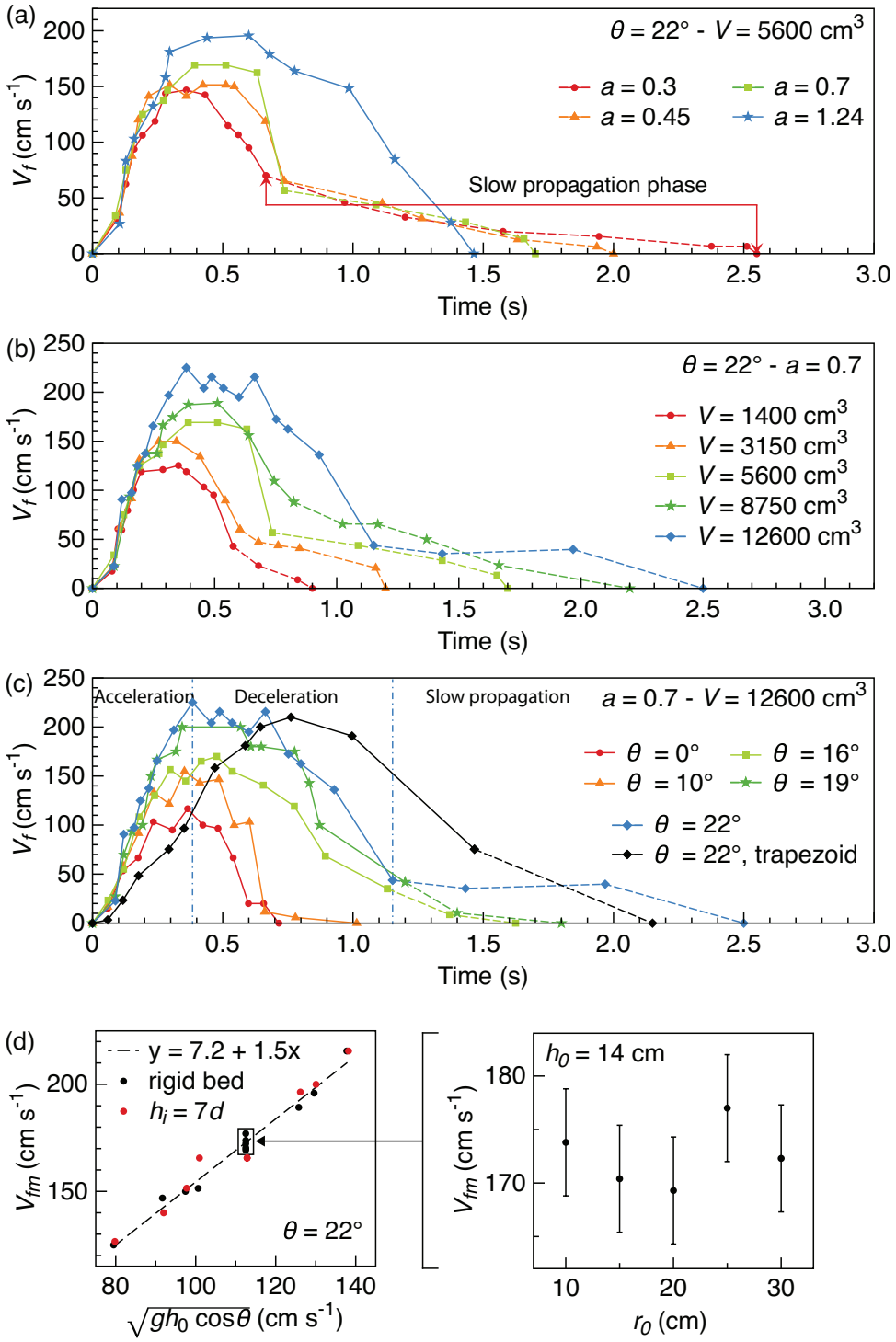

Figure 7. Flow front velocity $V_f(t)$ as a function of time, over the rigid bed, for (a) $\theta = 22°$, $V = 5600$ cm^3 and different column aspect ratios a; (b) $\theta = 22°$, $a = 0.7$ and different column volumes V; (c) $a = 0.7$, $V = 12600$ cm^3 and different slope angles θ and for $\theta = 22°$ with a rectangular and a trapezoidal column. The line is dashed during the slow propagation phase. In (c), the vertical dash-dotted lines separate the different phases of flow propagation for $\theta = 22°$. (d) shows the maximum front velocity V_{fm} as a function of $\sqrt{gh_0 \cos\theta}$ for $\theta = 22°$ and for $h_0 = 14$ cm and different column initial lengths r_0. Some values of V_{fm} for flows over an erodible bed of thickness $h_i = 7$ bead diameters d, for $\theta = 22°$, are given for comparison (red dots). Data in (d) are fitted by a linear function (dashed line). Error bars (not represented) are $\Delta V_f(t) = 10$ cm s^{-1} and $\Delta t = 0.06$ s.

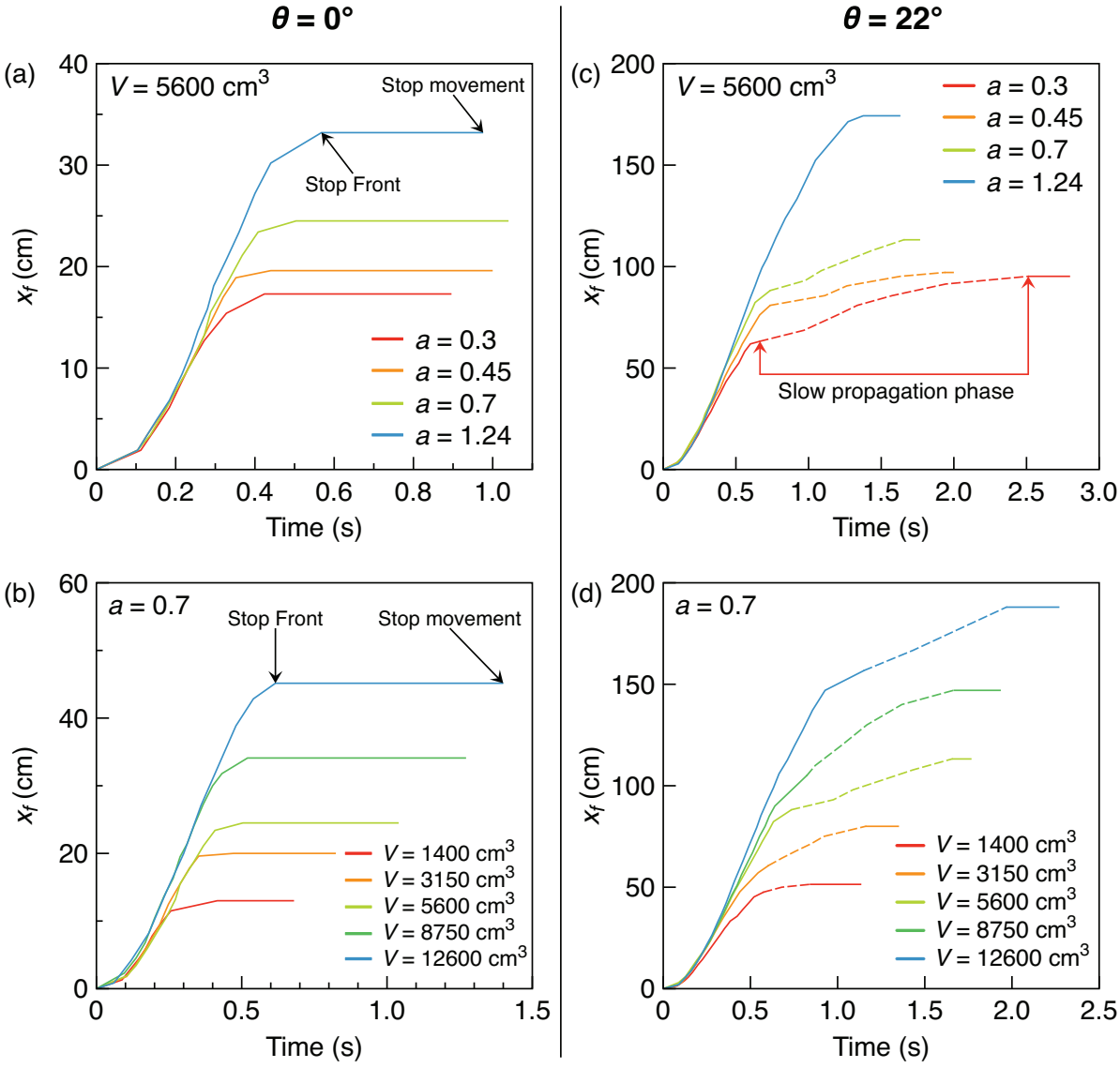

Figure 8. Position of the flow front from the gate x_f as a function of time, over the rigid bed and for different aspect ratios a and volumes V. (a) and (b) $\theta = 0°$; (c) and (d) $\theta = 22°$. The line is dashed during the slow propagation phase. Error bars (not represented) are $\Delta x_f = 3$ cm and $\Delta t = 0.06$ s.

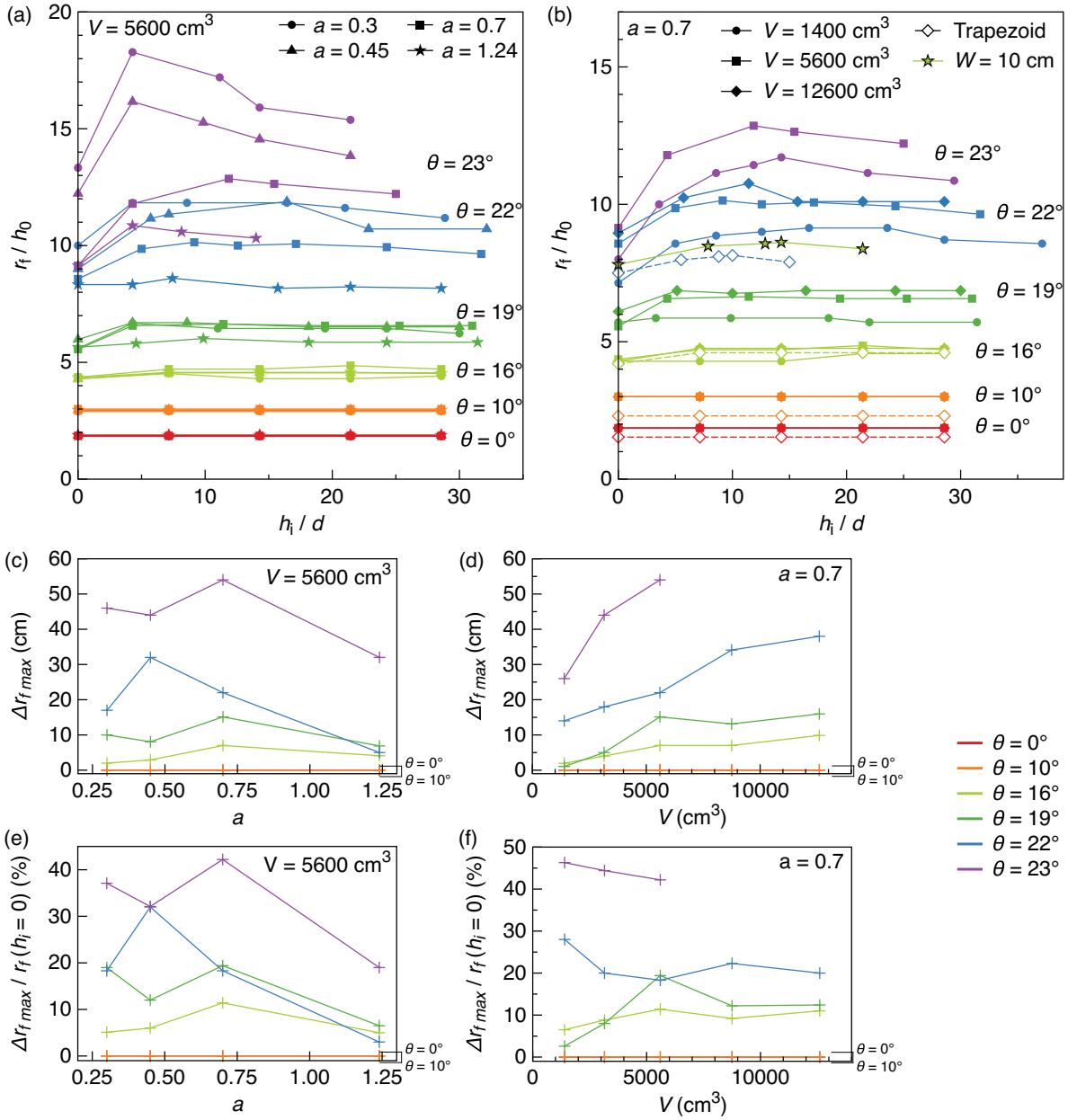

Figure 9. Normalized runout distance r_f/h_0 as a function of the erodible bed thickness h_i, scaled by the mean bead diameter $d = 700$ μm, for different slope angles (different colors). (a) $V = 5600$ cm^3 and different aspect ratios a, (b) $a = 0.7$ and different volumes V, with the trapezoidal column (empty diamond, $a = 0.7$ and $V = 12600$ cm^3) and for flows on the 10-cm-wide channel (green star, $h_0 = 21$ cm, $r_0 = 30$ cm, $a = 0.7$ and $V = 21 \times 30 \times 10 = 6300$ cm^3). The erodible beds in these experiments were built with the board method (see section 2). The differences of runout distances compared to flow over the rigid bed were calculated for the experiments in (a) and (b). Δr_{fmax} is the maximum of these differences versus all bed thicknesses h_i and is represented, for different slope angles θ, (c), (d) in absolute value and (e), (f) in % of the runout distance over the rigid bed $r_f(h_i = 0)$ as a function of (c), (e) the aspect ratio a for $V = 5600$ cm^3 and (d), (f) the volume V for $a = 0.7$.

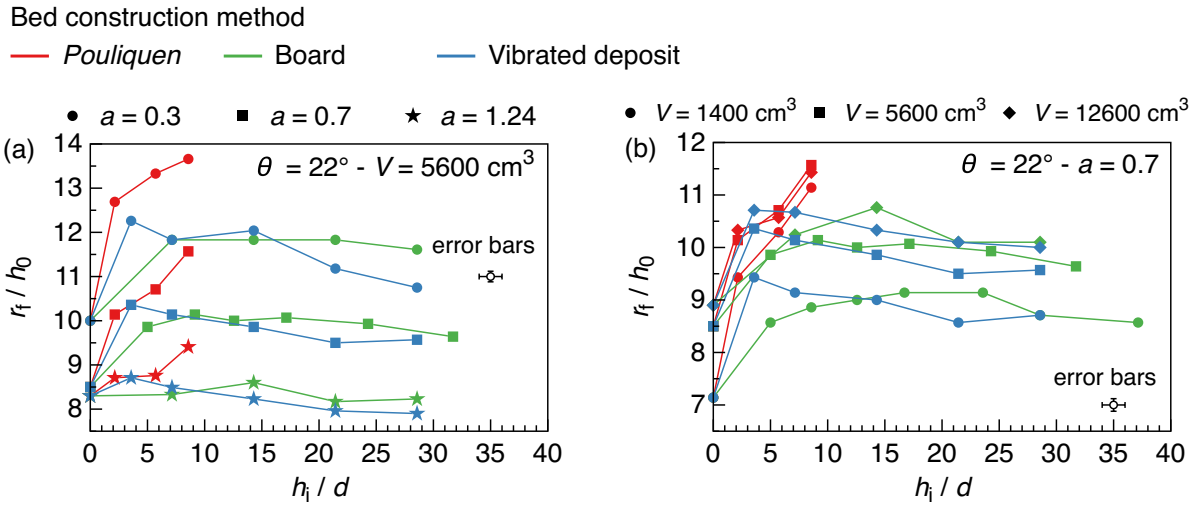

Figure 10. (a) and (b) are plots of the normalized runout distance r_f/h_0 as a function of the erodible bed thickness h_i, scaled by the mean bead diameter $d = 700$ μm, for $\theta = 22°$. Different methods leading to an increasing degree of compaction were used to build the erodible bed: the *Pouliquen*, board and bed vibration methods (see section 2). (a) is for $V = 5600$ cm^3 and different aspect ratios a and (b) is for $a = 0.7$ and different volumes V.

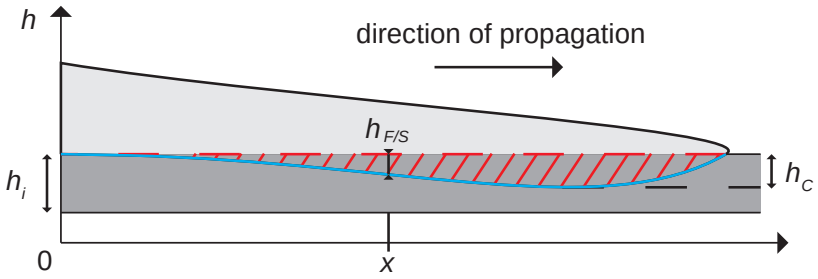

Figure 11. Schematic portrayal of the interface (blue) between the flowing (red cross-hatched) and static (dark grey) parts in the erodible bed of thickness h_i at the head of the avalanche (light grey). The position $h_{F/S}$ of the static/flowing interface is measured versus time at a fixed distance x from the gate. h_C is the maximum depth of excavation, i.e. the deepest position reached by the flowing/static interface $h_{F/S}$.

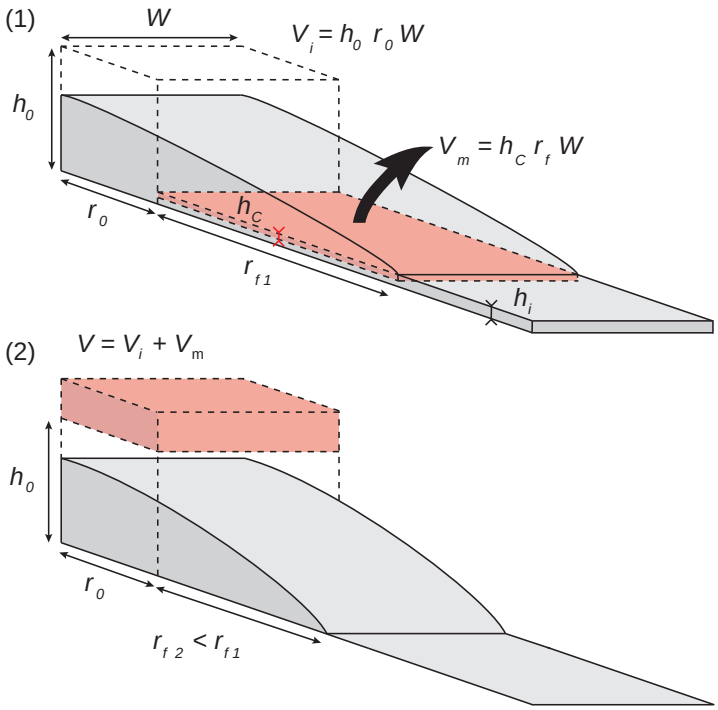

Figure 12. Illustration of the principle of the experiments conducted to test the potential effect of the addition of mass to the flow caused by bed erosion. The maximum volume V_m of the initially static bed put into motion by the flow is estimated (1) and added to the initial volume V_i for an experiment over the rigid bed (2). r_{f1} and r_{f2} are the runout distances obtained in the first and second experiments, respectively.

Table 3. Characteristics of the Experiments described in Figure 12 [a]

θ	a	V_i	h_i	h_C	V_m	r_{f1}	r_{f2}	$\frac{r_{f1}-r_{f2}}{r_{f1}}$
(°)	-	(cm^3)	(mm)	(mm)	(cm^3)	(cm)	(cm)	(%)
22	0.7	1400	10	2	256	64	54	15.6
23	0.7	1400	10	3	492	82	70	14.6
22	0.7	5600	3	2	552	138	126	8.7
22	0.7	5600	5	3	852	142	136	4.2
22	0.7	12600	1	1	420	210	196	7.0
22	1	2000	8	3	504	84	78	7.1
22	1	2000	10	3	510	85	78	8.2

[a] The runout distance r_{f1} of flows of volume V_i over an erodible bed of thickness h_i, with an estimated excavated volume $V_m = h_C r$ with a greater volume $V = V_i + V_m$ over the rigid bed, for different slope angles θ, aspect ratios a and volumes V.

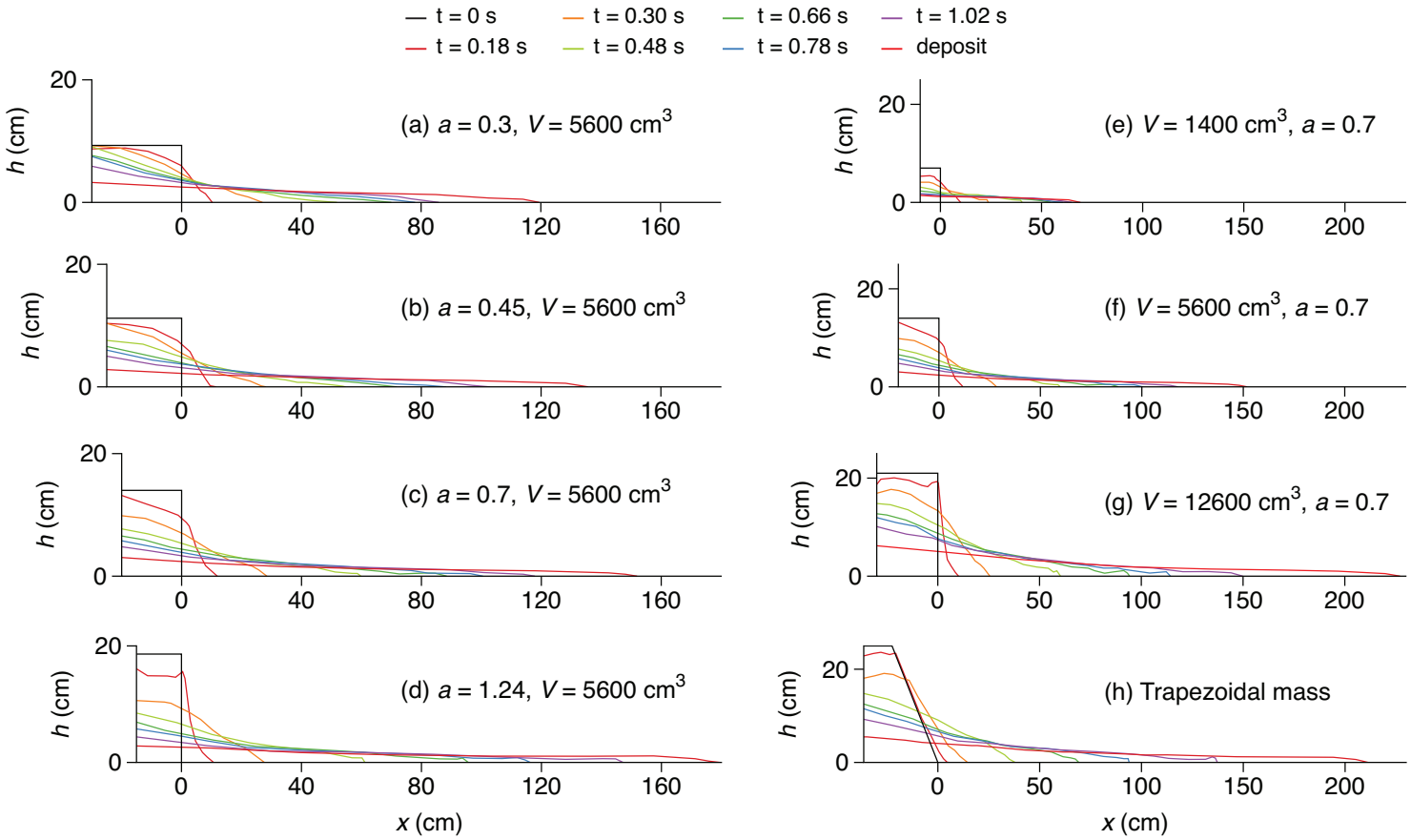

Figure 13. Different colored curves from top to bottom in each graph are thickness profiles $h(x,t)$ at different times t of the granular mass as a function of the downslope position x for flows over an erodible bed of thickness $h_i = 7d$ with $\theta = 22°$. (a)-(d) $V = 5600$ cm^3 and different aspect ratios a; (f)-(g) $a = 0.7$ and different volumes V and (h) trapezoidal column with $V = 12600$ cm^3 and $a = 0.7$.

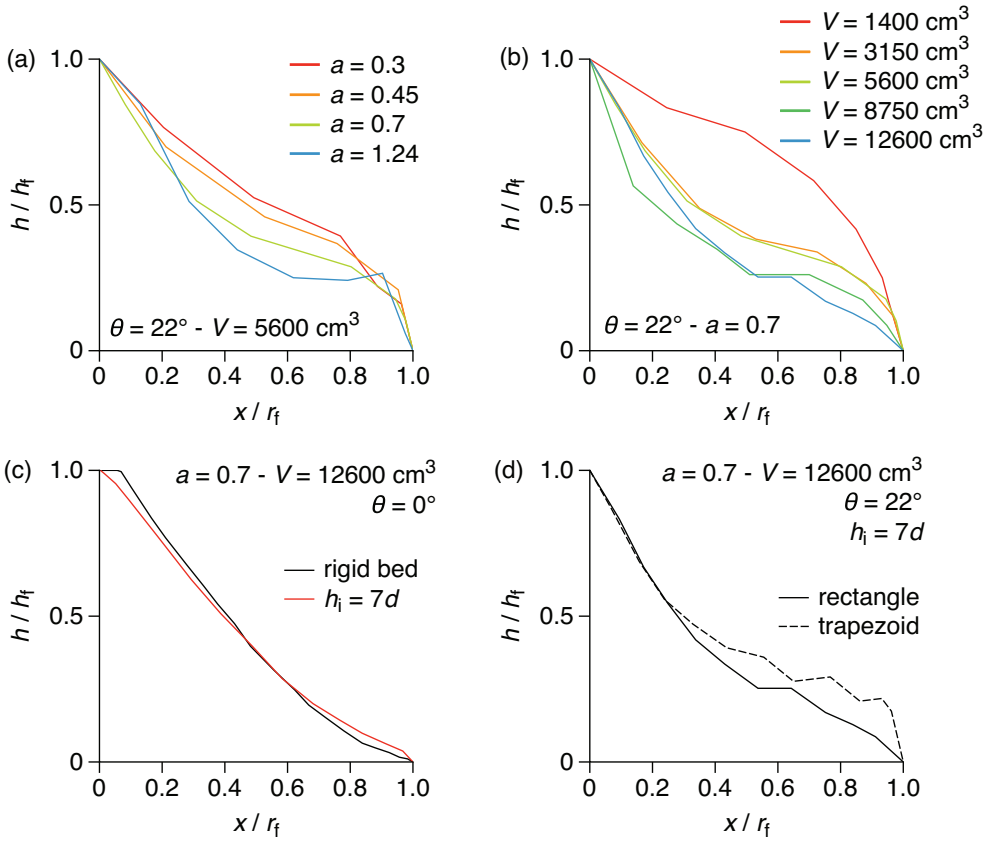

Figure 14. Final normalized thickness profiles of the deposit h/h_f as a function of the normalized downslope position x/r_f, over an erodible bed of thickness $h_i = 7d$ for: (a) $\theta = 22°$, $V = 5600$ cm^3 and different aspect ratios a; (b) $\theta = 22°$, $a = 0.7$ and different volumes V; (c) $\theta = 0°$, $a = 0.7$ and $V = 12600$ cm^3 with the deposit over a rigid bed; (d) $\theta = 22°$, $a = 0.7$ and $V = 12600$ cm^3 with both the rectangular and trapezoidal columns.

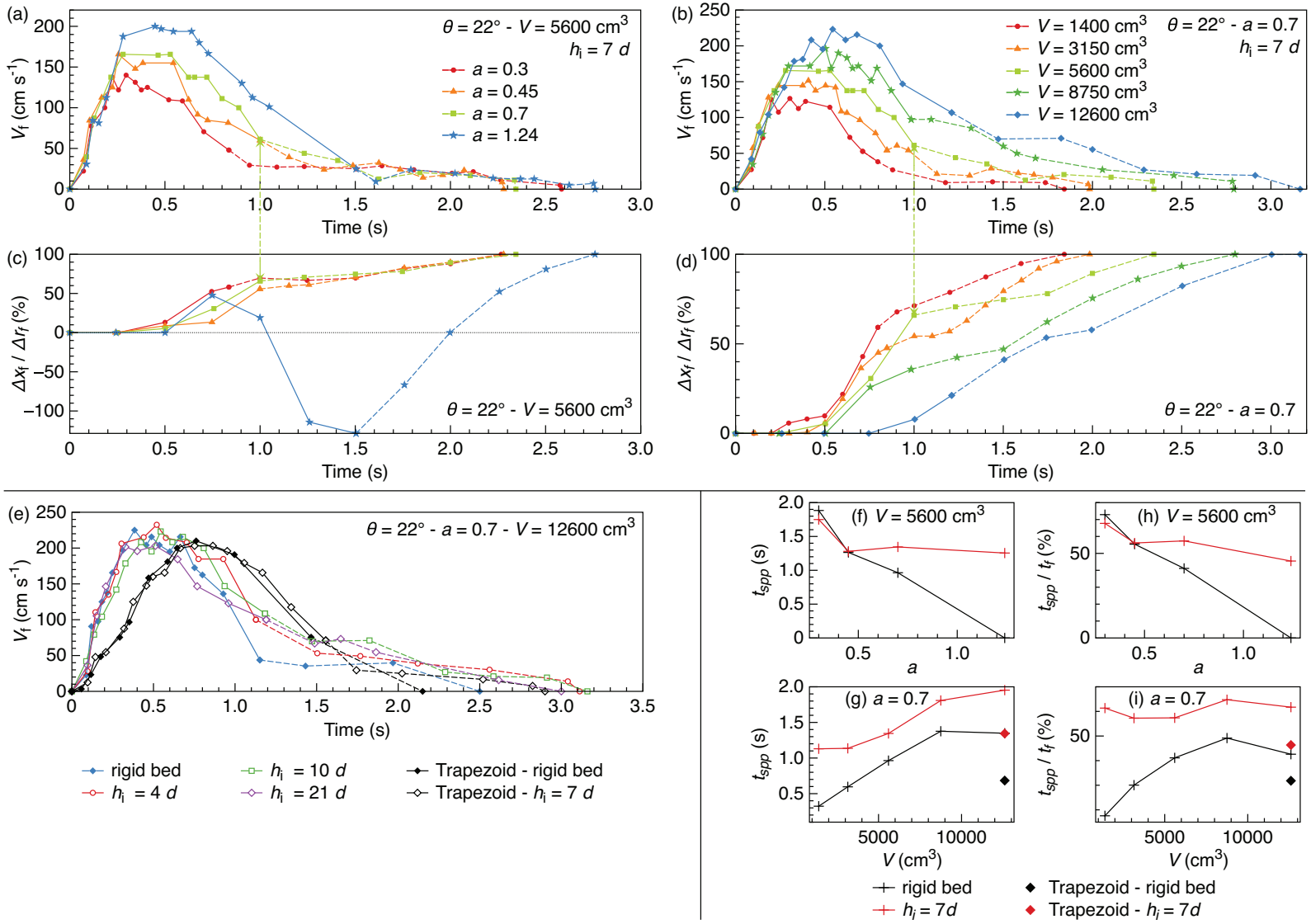
(a)
θ = 22° - V = 5600 cm3
hi = 7 d
a = 0.3
a = 0.45
a = 0.7
a = 1.24
Vf (cm s-1)
Time (s)
(b)
V = 1400 cm3
V = 3150 cm3
V = 5600 cm3
V = 8750 cm3
V = 12600 cm3
θ = 22° - a = 0.7
hi = 7 d
Vf (cm s-1)
Time (s)
(c)
Δxf / Δrf (%)
θ = 22° - V = 5600 cm3
Time (s)
(d)
Δxf / Δrf (%)
θ = 22° - a = 0.7
Time (s)
(e)
θ = 22° - a = 0.7 - V = 12600 cm3
Vf (cm s-1)
Time (s)
rigid bed
hi = 4 d
hi = 10 d
hi = 21 d
Trapezoid - rigid bed
Trapezoid - hi = 7 d
(f) V = 5600 cm3
tspp (s)
a
(h) V = 5600 cm3
tspp / tf (%)
a
(g) a = 0.7
tspp (s)
V (cm3)
(i) a = 0.7
tspp / tf (%)
V (cm3)
rigid bed
hi = 7d
Trapezoid - rigid bed
Trapezoid - hi = 7d

Figure 15. Flow front velocity $V_f(t)$ as a function of time over an erodible bed of thickness $h_i = 7d$ with $\theta = 22^\circ$ for: (a) $V = 5600$ cm^3 and different aspect ratios a; (b) $a = 0.7$ and different volumes V. (c) and (d) show the difference of the flow front position with respect to that over the rigid bed Δx_f normalized by the runout distance difference Δr_f as a function of time, for the flows in (a) and (b) respectively. (e) shows $V_f(t)$ for $\theta = 22^\circ$, $a = 0.7$, $V = 12600$ cm^3 and different bed thicknesses h_i, with a rectangular and a trapezoidal column. The line is dashed during the slow propagation phase. (f)-(i) Duration of the slow propagation phase t_{spp} of flows over the rigid bed (black line) and over the erodible bed (red line), (f), (g) in absolute value and (h), (i) in % of the total duration of propagation t_f for (f), (h) $V = 5600$ cm^3 and different aspect ratio a and (g), (i) $a = 0.7$ and different volumes V and also for the trapezoidal column with $V = 12600$ cm^3 and $a = 0.7$ (diamonds). Error bars (not represented) are $\Delta V_f(t) = 10$ cm s^{-1}, $\Delta t = 0.06$ s and $\Delta t_{spp} = 0.1$ s.

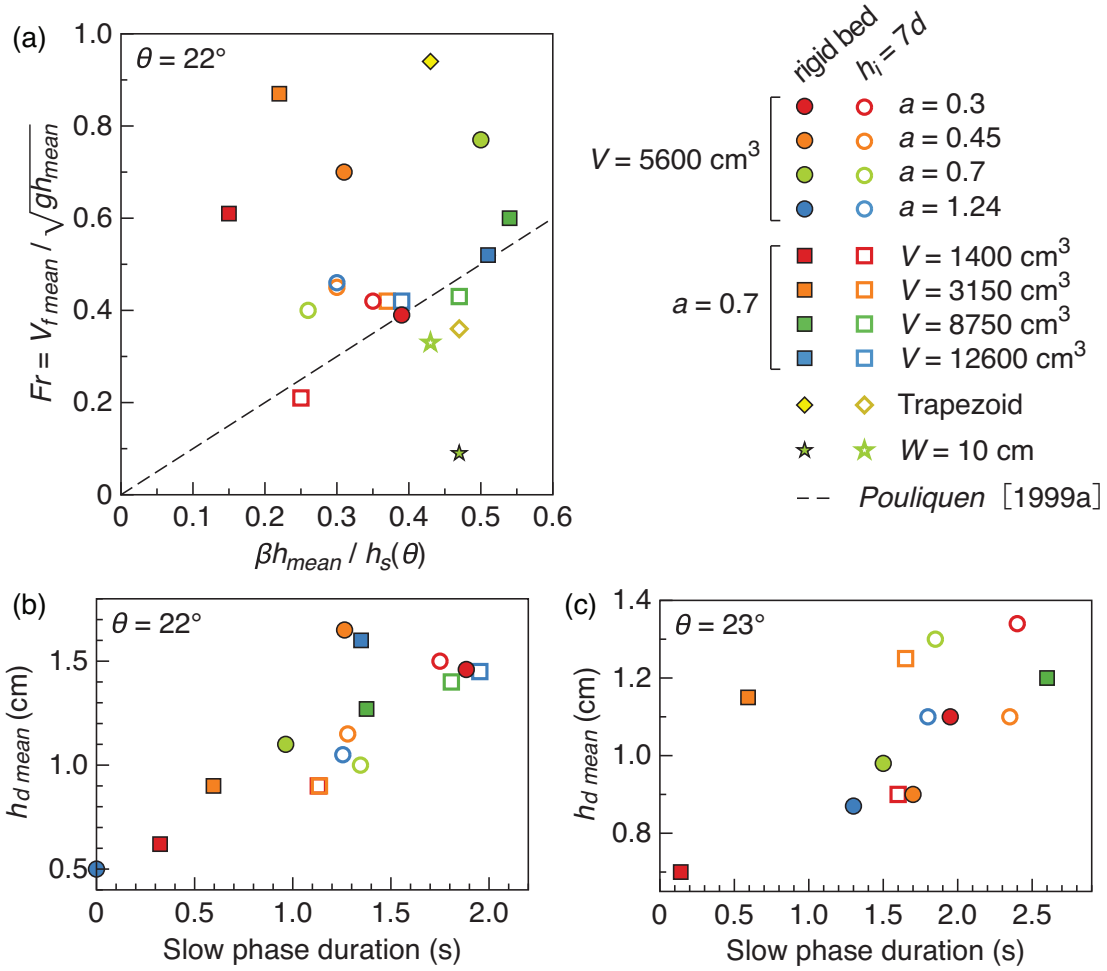

Figure 16. (a) Froude number $Fr = V_{fmean}/\sqrt{gh_{mean}}$ as a function of $\beta h_{mean}/h_s(\theta)$ for flows during their slow propagation phase, for $\theta = 22°$, over the rigid bed (full symbol) and over an erodible bed of thickness $h_i = 7d$ (open symbol). V_{fmean} is the mean front velocity during the slow propagation phase, h_{mean} the mean flow thickness behind the flow front, $h_s(\theta)$ the thickness of the deposit for $\theta = 22°$ and $\beta = 0.136$ an empirical parameter. The black dashed line represents the scaling law (7). (b) and (c) Mean thickness of the deposit h_{dmean} where the deposit is quasi-parallel to the slope as a function of the duration of the slow propagation phase t_{spp} for (b) $\theta = 22°$ and (c) $\theta = 23°$. For experiments where the slow propagation phase was not apparent (a) and when the flow did not form a deposit and left the channel ((b) and (c)), the corresponding data point is not shown. Error bars are $\Delta V_{fmean} = 10$ cm s^{-1}, $\Delta h_{mean} = 0.2$ cm, $\Delta h_{dmean} = 0.2$ cm and $\Delta t_{spp} = 0.1$ s.

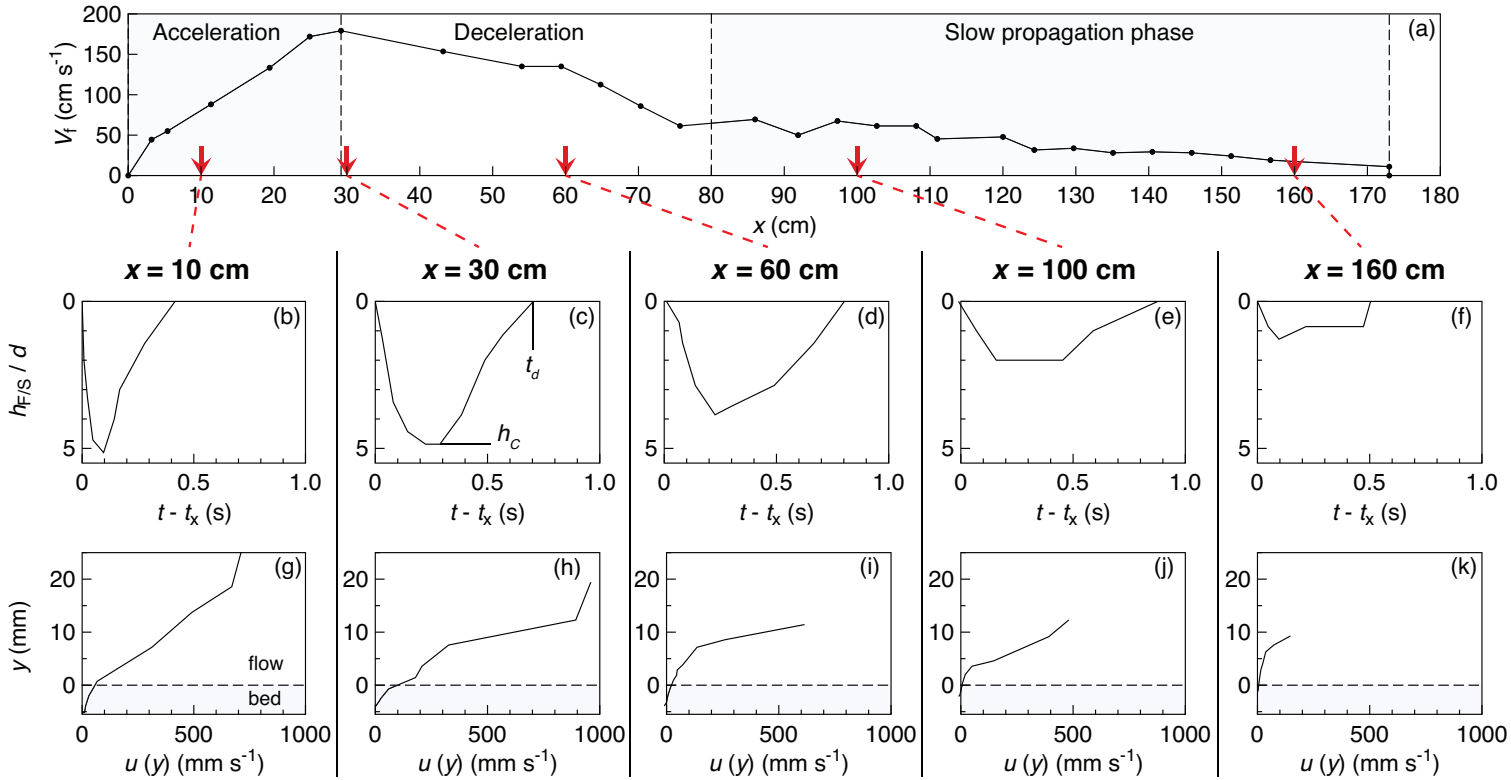

Figure 17. $\theta = 23°$, $V = 5600$ cm^3 and $a = 0.3$ over an erodible bed of thickness $h_i \simeq 7d$, where $d = 700$ μm is the mean bead diameter. (a) is a plot of the front velocity V_f as a function of the distance x from the gate. (b)-(f) show the vertical position of the flowing/static interface $h_{F/S}$ within the erodible bed as a function of time $t - t_x$. t_x is the instant when the flow front reaches the position x (red arrows). (g)-(k) show the internal velocity profile $u(y)$ on one side of the flow as a function of the elevation y above the channel base, at the same distances x from the gate, when $h_{F/S}$ reaches its maximum h_C. The dashed horizontal line represents the initial surface of the erodible bed. Error bars are $\Delta V_f = 10$ cm s^{-1}, $\Delta x = 3$ cm, $\Delta h_{F/S}/d = 1$, $\Delta t = 0.03$ s, $\Delta y = d$ and $\Delta u(y) \simeq 100$ mm s^{-1}.

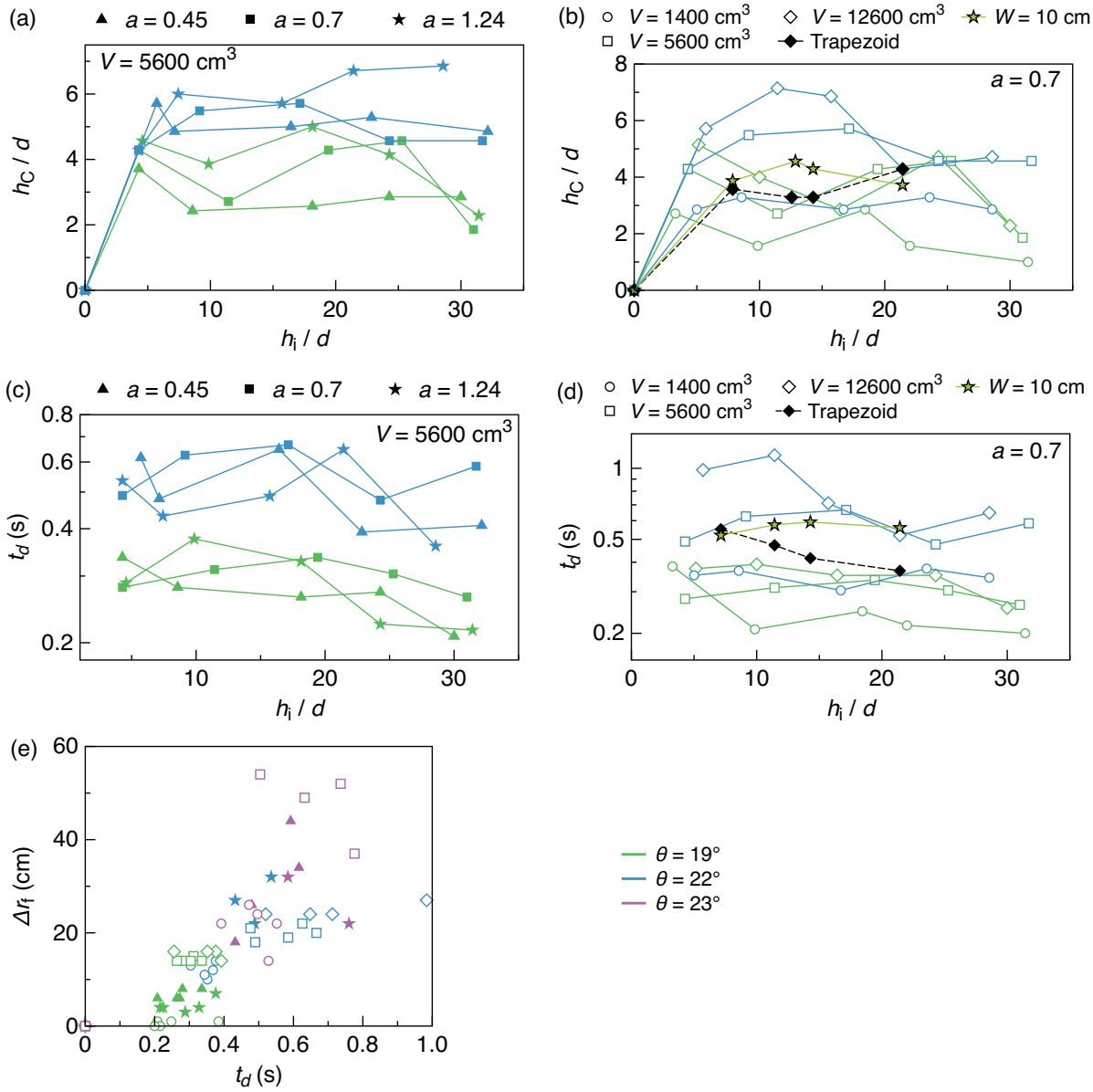

Figure 18. (a), (b) Maximum depth of excavation h_C (scaled by the mean bead diameter $d = 700$ μm) and (c), (d) duration of excavation t_d, as a function of the bed thickness h_i (board method), for $\theta = 19°$ (green) and $\theta = 22°$ (blue). (a) and (c) are for $V = 5600$ cm^3 and different aspect ratios a. (b) and (d) are for $a = 0.7$ and different volumes V. For $\theta = 22°$, data for flows obtained with the trapezoidal column (black diamond, dashed line, $a = 0.7$ and $V = 12600$ cm^3) and on the 10-cm-wide channel (green star, $h_0 = 21$ cm, $r_0 = 30$ cm, $a = 0.7$ and $V = 21 \times 30 \times 10 = 6300$ cm^3) are also represented. (e) Runout distance difference compared to that over the rigid bed Δr_f as a function of the duration of excavation t_d for different slopes angles θ (different colors) and for the experiments in (a)-(d) (same symbols). Error bars (not represented) for h_C, h_i are $\pm 1d$, $\Delta t_d = 0.1$ s and $\Delta(\Delta r_f) = 4$ cm.

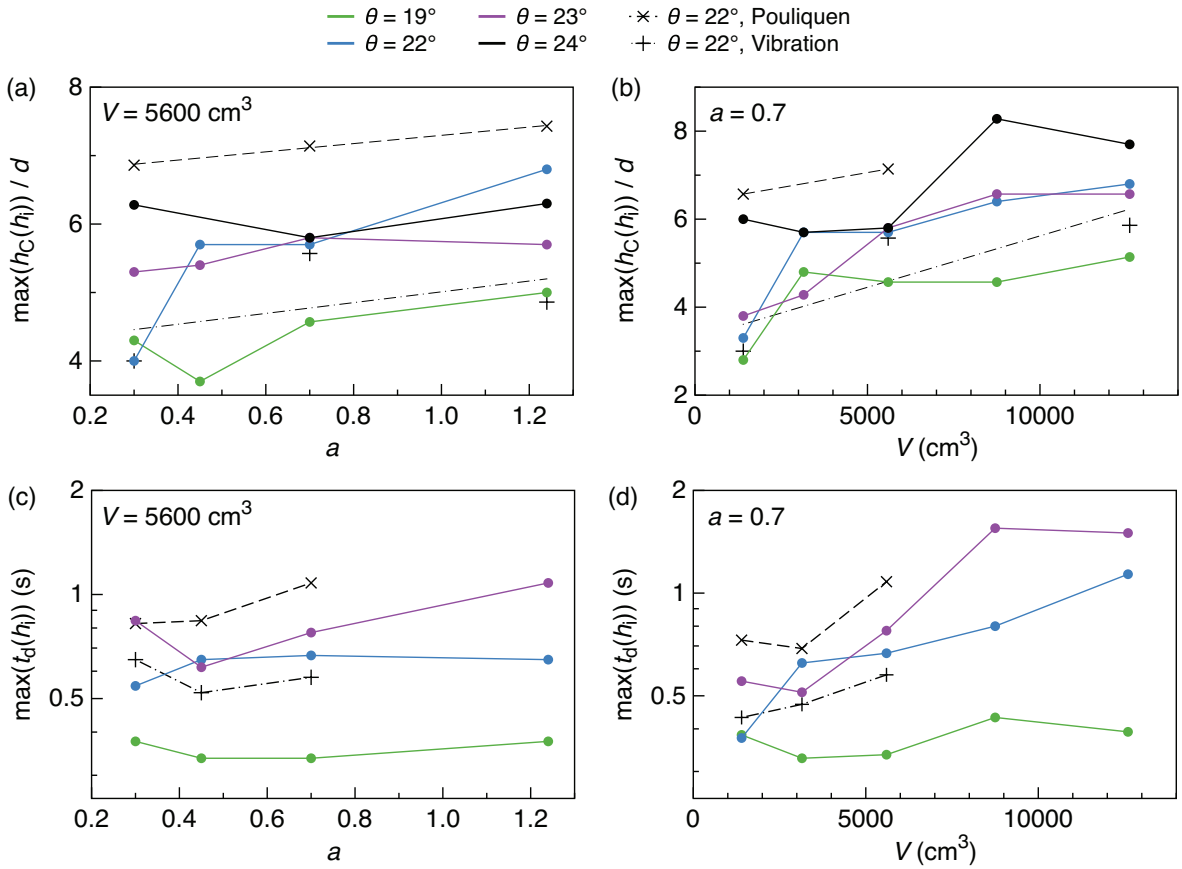

Figure 19. (a), (b) Maximum value of the maximum depth h_C for every bed thicknesses h_i investigated: $\max(h_C(h_i))/d$ as a function of (a) the aspect ratio a for $V = 5600$ cm^3 and (b) the volume V for $a = 0.7$, for different slope angles θ (different colors) and for $\theta = 22^\circ$ and the different methods of bed compaction: board (blue), *Pouliquen* ($\times$) and vibration ($+$). (c), (d) Maximum value of t_d over the thicknesses h_i: $\max(t_d(h_i))$ for different slope angles θ and different compaction methods (c) for $V = 5600$ cm^3 and different aspect ratios a and (d) for $a = 0.7$ and different volumes V. Error bars (not represented) for $\max(h_C(h_i))$ and h_i are $\pm 1d$ and $\Delta \max(t_d(h_i)) = 0.1$ s.

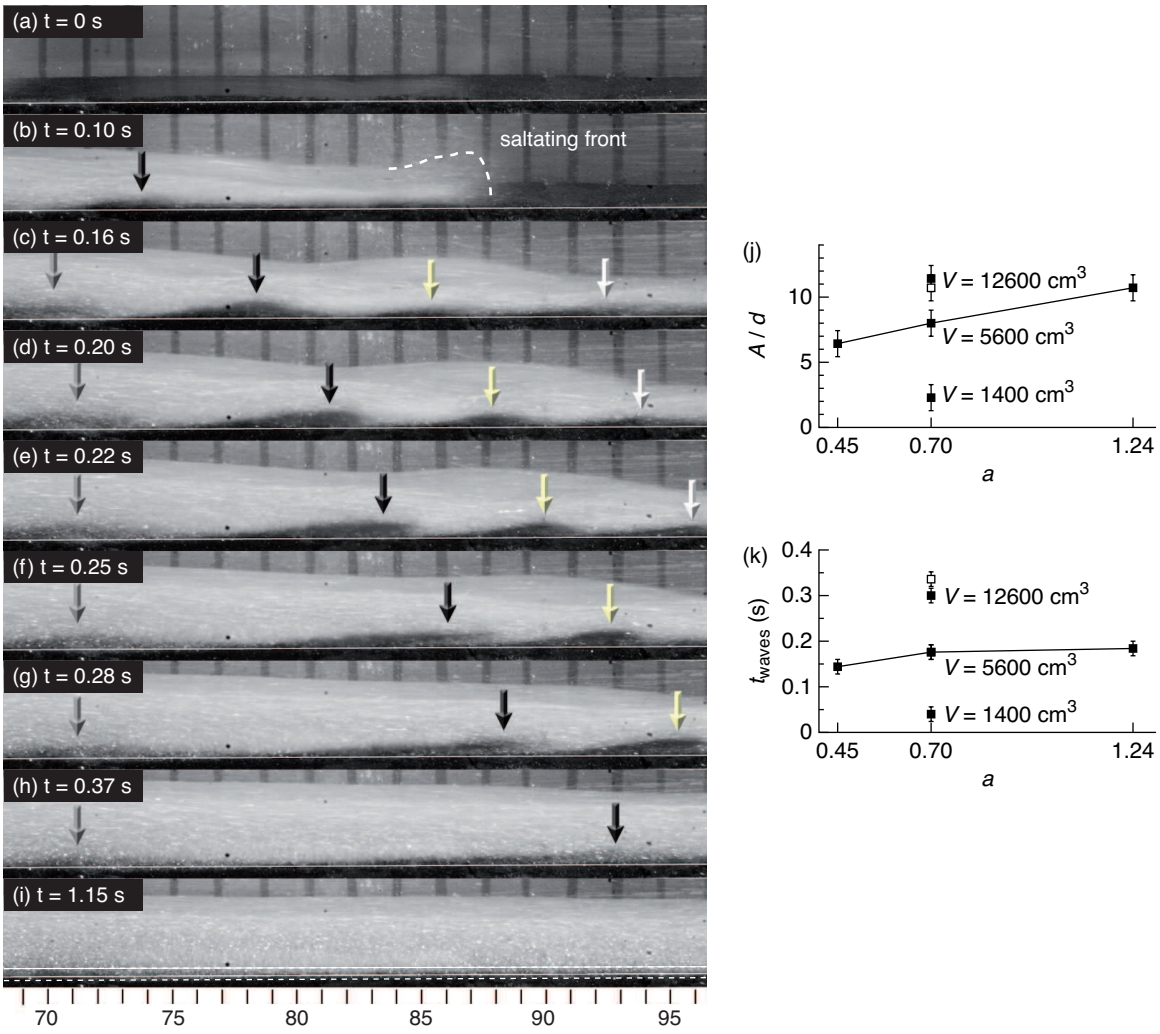

Figure 20. (a)-(i) Snapshots for values of x between 70 cm and 95 cm from the gate used to spread a volume $V = 12600$ cm^3 of white beads over an erodible bed of thickness $h_i = 5$ mm made of black beads, for $\theta = 24.5^\circ$ and $a = 0.7$. In (a), the top of the erodible bed is delimited by the white line. Vertical arrows indicate the propagation of three successive waves appearing at the interface between the erodible bed and the flow. (i) is a snapshot of the final deposit in which white and black beads are mixed within a thickness of 2.0 ± 0.5 mm at the interface of the erodible bed (black) and the flow deposit (white). (j) shows the maximum amplitude A of the erosion waves, scaled by the mean bead diameter d, for $\theta = 22^\circ$ (solid square) and for different aspect ratios a and volumes V. (k) is a plot of the duration t_{waves} of waves passing at the position of measurement for different values of a and V. The maximum amplitude and duration of waves for the experiment with $\theta = 24.5^\circ$, $a = 0.7$ and $V = 12600$ cm^3 is also represented (open squares).

Table 4. Notations

A	Maximum amplitude of the erosion waves
d	Mean diameter of the glass beads $d = 700$ μm
g	Gravitational acceleration
h_0, r_0, a, V	Initial height, downslope length, aspect ratio (i.e. h_0/r_0) and volume of the released granular column
h_C	Maximum value of $h_{F/S}(t)$
$h_{F/S}(t)$	Position (perpendicular to the slope) of the interface between the flowing and static grains
h_i	Thickness of the erodible bed
h_{mean}, h_{dmean}	Mean flow thickness behind the flow front and mean thickness of the deposit where the deposit is quasi-parallel to the slope
$h_s(\theta)$	Thickness of the bed formed at slope angle θ (see section 2)
$h(x,t), u(x,t)$	Thickness and velocity profiles of the flowing granular mass in the downslope direction
$\tilde{h}(x,t), \tilde{u}(x,t)$	Normalized thickness and velocity profiles of the flowing granular mass in the downslope direction
K	Ratio of vertical to horizontal stress
k	Empirical parameter in scaling laws
l, m	Length and mass of the slice of erodible bed removed to measure its volume fraction (see section 2)
r_f, h_f	Runout distance and final maximum thickness of the deposit
r_{f1}, r_{f2}	Runout distance obtained after the collapse of a granular column of volume V_i over an erodible bed and of volume $V_i + V_m$ over the rigid bed
t_d	Duration of bed excavation
t_f	Time at which the front stops
t_{spp}	Duration of the slow propagation phase
t_{waves}	Duration of the erosion waves
$u(y)$	Profile of downslope velocity measured on one side of the flow
v_1, v_2	Velocities of the upper (1) and lower (2) fluids in the Kelvin-Helmholtz instabilities
$V_f(t)$, V_{fm}	Front velocity and maximum front velocity
V_{fmean}	Mean front velocity for flows during their slow propagation phase
V_m	Maximum volume entrained by a given flow over an erodible bed
W	Width between channel sidewalls
x, y	Coordinates in the downslope direction and in the direction perpendicular to the slope
x_f	Front position in the downslope direction
β	Empirical parameter equal to 0.136 for glass beads
δ	Empirical friction angle in scaling laws
Δr_f, Δr_{fmax}	Runout distance difference obtained over an erodible bed compared to the case over a rigid bed and maximum value of this difference over the bed thicknesses h_i
$\Delta x_f(t)$	Difference of front position at instant t over an erodible bed compared to that over the rigid bed
ϵ	Dimensionless parameter defined by $\epsilon = (\tan\delta - \tan\theta)/a$
θ	Slope angle
θ_i	Slope angle related to the friction coefficient $\mu_i = \tan\theta_i$
θ_c	Critical slope angle separating two different dynamic regimes
θ_r, θ_a, θ_{rb}	Repose angle and avalanche angle of the glass beads and repose angle of the colored glass beads
λ	Erosion wave wavelength
μ	Friction coefficient
μ_1, μ_2, L	Parameters in equation (8)
ν, $\nu_{Pouliquen}$, ν_{board}, ν_{vib}	Solid volume fraction and mean solid volume fractions of erodible beds built with the Pouliquen, board and vibration methods
ρ, ρ_b	Density of the granular flow and of a glass bead
τ_c	Characteristic time
Φ_1, Φ_2	Granular concentrations of the upper (1) and lower (2) fluids in the Kelvin-Helmholtz instabilities